The effect of water and pressure on fabric development in olivine

Joshua Muir [1,2]*, Richard Skelton[2] and Andrew Walker[2,3],

1) Institute of Geochemistry, Chinese Academy of Sciences, 99 West Lincheng Road, Guiyang, Guizhou 550081, China
2) School of Earth and Environment, University of Leeds, LS2 9JT, United Kingdom
3) Department of Earth Sciences, University of Oxford, South Parks Road, Oxford OX1 3AN, United Kingdom

Word count:**7430**

Abstract:

Water has a very strong effect on both the strength and fabric development of forsterite but the mechanism of this effect is unclear. In the paper we use Density Functional Theory Peierls-Nabarro modelling to examine the effect of water on the Peierls stress of different forsterite slip systems. We find that water in Mg vacancies will weaken [100](010) slip and thus produce A fabrics while water in Si vacancies weakens [001](100) slip and thus produces C fabrics. With a combination of DFT and forcefield based methods we find that while in the bulk hydrated vacancies typically occur as M1>M2>Si, near the [100] and [001] screw dislocation cores they occur as Si>M2>M1. Thus by simple modification of the Peierls stress and by segregation of Si vacancies to dislocations, water enhances C fabrics in forsterite. This production is enhanced by pressure and should be independent of water concentration above ~90 ppm H/Si in perfect forsterite. The shape of dislocations is not significantly modified by water and thus the stress exponent of dislocation glide should be unaffected. Water additionally reduces the activation volume of the Peierls mechanism by ~5 times by changing the pressure dependence of slip. E fabrics cannot be produced by a dislocation creep mechanism due to the consistently high Peierls stress of the [100](001) slip system and thus require another deformation method to form.

Introduction:

Olivine is a major component (40-80%) of the Earth's upper mantle and thus understanding its deformation is critical for understanding upper mantle rheology. The plastic deformation of olivine, however, is very complex and not fully understood and the effect of water on this deformation adds further complexity. Olivine can dissolve large quantities of water (up to ~30,000 ppm H/Si depending on pressure (Hirschmann, 2006)) with the water content of the deep asthenosphere estimated from conductivity data to be around 1,500±800 ppm H/Si (Wang et al., 2006, Karato, 2011) but with heterogeneous distribution of between 0-10,000 ppm H/Si (Yoshino et al., 2006, Karato, 2011).

Of particular importance is the effect of water on the development of olivine LPO fabrics. Olivine has 4 major fabrics labelled A, B, C and E arising from predominant slip systems [100](010), [001](010), [100](001) and [001](001) respectively. Deformation experiments have shown that generally olivine forms an A fabric but increasing the pressure of the stress can induce the formation of B fabrics (Raterron et al., 2009, Raterron et al., 2007, Raterron et al., 2011, Raterron et al., 2012, Bollinger et al., 2016, Jung et al., 2009, Ohuchi et al., 2011). Similarly the introduction of water has been shown to induce the formation of E or C fabrics (Jung and Karato, 2001, Jung et al., 2006, Katayama et al., 2004, Ohuchi and

Irifune, 2014). All of these papers show, however, that fabric transitions in olivine possess a complex interplay between water content, pressure and stress/temperature that is not yet fully understood. Concluding information about deformation mechanics from natural rocks is difficult due to a lack of information about their deformation environments and histories but in general there is a weak trend of C fabrics being found in wet rocks (which supports water inducing an A to C fabric change) and B fabrics being found in rocks from convergent boundaries (which supports stress inducing an A to B fabric change) while rocks with E fabrics are relatively rare (Karato et al., 2008b, Michibayashi et al., 2016, Jung, 2017).

Understanding texture development in olivine is important because different olivine fabrics have different seismic anisotropies and thus changes in olivine fabric preference will change the flow properties of the upper mantle. The presence and the change of olivine fabrics has been used to explain various properties of the upper mantle including the decrease in seismic anisotropy and the sign change of V_{SH}-V_{SV} with depth (both indicative of an A to B/C transition) (Ohuchi and Irifune, 2013, Ohuchi and Irifune, 2014, Raterron et al., 2012, Ohuchi et al., 2011), the larger anisotropy in continental vs oceanic lithosphere (related to the depth of the A to B transition) (Raterron et al., 2012), the conversion of shear wave splitting from trench parallel near the trench to trench perpendicular near the back arc in colder wetter slabs (conversion from A/C to B) (Jung et al., 2006, Karato et al., 2008a, Ohuchi et al., 2012, Katayama and Karato, 2006, Kneller et al., 2005, Kneller et al., 2007) and finally the overall anisotropy and shear wave splitting direction of the upper mantle (predominately A or E fabric) (Karato et al., 2008b). Thus knowledge of the effect of water on these transitions is essential to constraining the amount of water in the upper mantle, its overall distribution and the anisotropy and thus the flow of the upper mantle.

The mechanism for how water changes fabric texture in forsterite, however, is unclear as is the interaction of this mechanism with pressure and stress. A major complication in determining this mechanism is the complex nature of forsterite deformation with upper mantle conditions being conducive to both dislocation and diffusion creep with the latter favoured by lower temperatures, smaller grains sizes and lower stresses (Faul et al., 2011, Ohuchi et al., 2017, Fei et al., 2016, Katayama and Karato, 2008, Wang, 2016, Kawazoe et al., 2009). Dislocation creep is likely dominant in the asthenosphere and diffusion creep in the lithosphere (Fei et al., 2016) but both deformation mechanisms will likely carry strain under most conditions (Nishihara et al., 2014) and dislocation glide is possible at even quite low temperatures and stresses (~800 K <200 MPa) (Boioli et al., 2015b). In this paper we shall address the viability of one of the most straightforward ways that water could affect fabric evolution- by changing the Peierls stress (ease of dislocation glide) of different slip systems (Mackwell et al., 1985, Katayama and Karato, 2008) and thus changing which slip systems carry the most strain. We shall do this by using atomistic Peierls-Nabarro calculations to model the different slip systems and to calculate their Peierls stress. Previous work (Skelton and Walker 2017) has shown that vacancies can reduce the Peierls stress of different slip systems in different amounts but this work does not consider the effect of hydration on vacancies and only considers the [100](010) and [001](010) slip systems. In this work we shall consider the effect of both bare and hydrated vacancies on [100](010), [001](010), [100](001) and [001](100) slip systems while also considering the effect of pressure which is experimentally hard to constrain while also controlling water fugacity.

Methods

To establish the effect of water on fabric development in forsterite two things need to be established- the position of the water in the crystal and its effect on the forsterite slip systems. To establish the former we calculated the energies of dry and hydrated Mg and Si vacancies in a forsterite bulk (using Density Functional Theory (DFT)) and near a dislocation core (using forcefields). To examine the latter point we calculated the Peierls stress of [100](010), [001](010), [001](100) and [100](001) slip systems in forsterite at 0, 5 and 10 GPa in the bulk crystal and with hydrated and non-hydrated M1, M2 and Si vacancies. To do this we used DFT calculations to calculate elastic constants and Generalised Stacking Faults (GSF) of forsterite and then used the Peierls-Nabarro (PN) approximation to calculate the dislocation widths and Peierls stresses. Peierls stresses were then converted to fabric textures using an LPO evolution code (D-Rex).

DFT Calculations

DFT calculations were used to calculate vacancy energies in bulk forsterite, elastic constants in bulk forsterite and GSF energies for PN calculations. Calculations were done with the CASTEP code (Clark et al., 2005). PBE pseudopotentials were as generated on-the-fly by CASTEP 16.11- the valence shells are Mg 2s, 3p and 3s O 2s 2p, Si 3s 3p and H 1s.

To calculate the energies of vacancies and the elastic constants a (2x1x2) forsterite super cell was used with a plane wave cut off of 1000 eV, (4x4x4) k-points and relaxed to a force tolerance of 0.01 eV/Å and an energy tolerance of 1x10^{-5} eV/atom. A (2x1x2) supercell was used to ensure that there was roughly 10 Å between repeating vacancies in all directions.

A (4x2x4) supercell was also tested and the vacancy energy changed by <0.01 eV. While hydrated vacancies are chargeless, dry vacancies are charged and so the energy produced by DFT includes a defect-defect interaction term while we require the energy of a defect in infinite space which would not include such a term. We can correct for this by assuming our system is an array of point charges in a neutralising background charge as outlined in Leslie and Gillan (1985) and previously used for forsterite by Brodholt and Refson (2000). To use this method the relative permittivity of the cell needs to be set - we used a value of 6.2 following Brodholt and Refson (2000).

To create the energy of dry vacancies an Mg^{2+} or a Si^{4+} ion was removed and a corresponding charge added to the system. There are two non-equivalent Mg sites in olivine (M1 and M2) and we examined vacancies in both of these sites. To create the energy of hydrous vacancies we removed an Mg^{2+} or a Si^{4+} ion and replaced it with 2 or 4 H^+. In every case the hydrogen atoms are bound to an O within the vacancy and then hydrogen bonded to another oxygen also within the vacancy. When considering the position of the H and not its orientation in the perfect bulk case there are 4 possible arrangements of hydrogen in a Mg vacancy and 1 in a Si vacancy. When we consider the breakdown of symmetry caused by a glide plane there are 9 possible arrangements in the Mg vacancy. Arranging the hydrogens on different sites causes a large difference in possible energies with the most unstable arrangement being 0.9 eV more unstable than the most stable one. In both an M1 and M2 vacancy the most stable arrangement has 2 hydrogens on adjacent oxygen atoms in the equatorial plane of the octahedron. For energy difference calculations we used the most stable arrangement of hydrogen in each vacancy (with the effect of other arrangements discussed in the text) and for GSF calculations we started the hydrogen in the most stable arrangement but allowed it to relax freely after unit cell displacement. For our treatment of configurational entropy of these vacancies see the supplementary methods.

To calculate elastic constants we applied 3 different strains with 12 different magnitudes ranging from -0.2 to 0.2 to our unit cells and then fit the resulting stress-strain curves with 2nd order polynomials.

To calculate the GSF large slabs are needed. A base (2x1x2) unit cell was chosen and then repeated 12 times in the surface normal direction when the surface normal was along [100] or [001] and 8 times when the surface normal was along [010]. These values were both found to be necessary to converge GSF maxima to <5 meV/ Å^2. In all cases a vacuum of 8 Å was introduced to the bottom of the cell to limit surface-surface interactions to a single interface. For these large slabs lower cutoffs were used with plane wave cutoffs of 850 eV at the gamma point with forces converged to 0.05 eV/Å and energy convergences of 2x10^{-5} eV/atom. In these calculations we are finding the energy difference of successive displacements and so error cancellation means lower cutoffs are sufficient to produce GSF curves.

Vacancy Segregation

To calculate the energy of vacancies at a dislocation core it is necessary to model the core which requires 10,000s of atoms and thus is beyond the scope of DFT. Instead we use interatomic potentials to calculate the energy of the segregation of vacancies from a bulk like environment (where their energy is calculated by DFT) to the region of a dislocation core. To do this we used the same methods and core structures as work (Skelton and Walker 2017) but we modelled Si vacancies rather than Mg vacancies. This method is outlined in more detail in the supplementary methods and in work (Skelton and Walker 2017) but in essence a dislocation core was constructed using the disloPy code (https://github.com/andreww/disloPy/) and then the energy of a dry or hydrated Si vacancy is calculated at all possible sites relative to the dislocation core up to a set distance away (12.5 Å). Energies were calculated using a forcefield designed for hydrated olivine (Wright and Catlow, 1994, Lewis and Catlow, 1985, Schroder et al., 1992) (Table S1) and the GULP code (Gale, 1997).

Peierls-Nabarro Method:

To calculate the dislocation structures and Peierls stress we use the Peierls-Nabarro method (Nabarro, 1947). This is an approximate method which represents a dislocation as a series of partial dislocations across a glide plane with the assumption that the dislocation is collinear. The dislocation is then composed of two forces- the linear elastic response of the crystal and the energy of inelastic misfit- which balance at equilibrium. The traditional PN formulation requires a continuous dislocation density which is computationally difficult to calculate and so instead we use a semi-discrete PN formulation (Bulatov and Kaxiras, 1997) which allows us to calculate the dislocation density at a series of isolated points which can be run as isolated computations. The PN calculations were done using the disloPy code (https://github.com/andreww/disloPy/) which has been previously documented in Skelton and Walker (2017) and the equations used and the general workflow is outlined in our supplementary methods. In brief, we need to calculate the inelastic misfit energy (E_{misfit}) and the linear elastic response energy ($E_{elastic}$) from which a dislocation is constructed by minimising its total energy. Once a dislocation structure is obtained, the Peierls stress can be calculated by increasing the value of an applied stress to the system until the equations break down. Both $E_{elastic}$ and E_{misfit} are calculated using DFT with the $E_{elastic}$ calculated by elastic constant calculation and E_{misfit} calculated via GSFs.

GSF calculations are performed by creating a large slab and then moving half of the slab relative to the other half various distances along the dislocation vector. Displacement is done in successive amounts from x=0 to x=burgers vector with 20 points used for systems with an [100] burgers vector (successive displacements increased by ~0.24 Å) and 26 points for an [001] burgers vector (displacements increased by ~0.3 Å). Such a dense grid of points is required because minor variations in the shape of the GSF curves can strongly affect the final fitting and thus the Peierls stress. At each displacement point the atomic positions are relaxed but to keep displacement fixed to the appropriate point along the dislocation vector the movement of Mg and Si is fixed so that they can only relax along the surface normal. The movement of O is not restricted so that SiO_4 tetrahedra can rotate to minimise the energy. The movement of H is not restricted so that hydrogen can move about the vacancy to find the minimum energy. Once all displacements have been calculated a γ-line can be constructed to use in PN calculations. The minimum energy slip plane was found by trial and error in no vacancy slip systems. Vacancies were always introduced as close to the slip plane as possible.

An additional consideration concerns the effect of breaking the symmetry of the hydrated vacancy during displacement and thus introducing entropy barriers. This concern is addressed in the supplementary information and is found to be negligible.

D-Rex Calculations

To produce illustrative fabric diagrams we used the D-Rex approach (Kaminski et al., 2004) as implemented by C. Thissen (https://github.com/cthissen/Drex-MATLAB/). This is a kinematic model for simulating texture development through considering energy reductions of an averaged field (rather than individual grains) using dynamic recrystallization, subgrain rotation and grain-boundary migration which are all set parameters. In all cases 1000 particles were used, final shear was set to 1 and our velocity gradient tensor was $l = \begin{pmatrix} 0 & 1 & 0 \\ 0 & 0 & 0 \\ 0 & 0 & 0 \end{pmatrix}$. There are three crucial parameters in D-Rex- M* which represents the migration of grain boundaries, λ* a dimensionless nucleation parameter and χ which controls the rotation of grains- following Kaminski (2002) we set these to suitable dry forsterite values of 50, 5 and 0.3 respectively. While wet forsterite likely has significant difference in these values these were fixed simply to demonstrate how changes in Peierls stress alone can lead to water induced fabric development. For a more definitive effect on fabric development proper exploration of these values will be required. It is also required to set the critical relative shear stress (CRSS) for the four different slip systems. For each of our calculations these were set to the screw Peierls stresses at the appropriate conditions that we determined through our calculations. The stress exponent was fixed to 3.5 for all slip systems.

Results

Hydrated Vacancies in Forsterite:

Before we can comment on the effect of water on forsterite slip systems we need to know where the water exists in the crystal. Water distribution in olivine and forsterite is a complex problem but 4 major sites of water have been determined that are (in Kroger-Vink notation) $(2H)_{Mg}^{X}, (4H)_{Si}^{X}, (1H)_{Mg}^{\prime}Fe_{Mg}^{\cdot}$ and $Ti_{Mg}^{\cdot\cdot}(2H)_{Si}^{\prime\prime}$ (see for example Tollan et al. (2018), Le Losq et al. (2019) and Walker et al. (2007)). In this work we shall examine only hydrated Mg $(2H)_{Mg}^{X}$ and Si $(4H)_{Si}^{X}$ vacancies. There are a few reasons for this choice. First $(2H)_{Mg}^{X}$ and $(4H)_{Si}^{X}$ vacancies will always be present in forsterite whereas $(1H)'_{Mg}Fe^{\cdot}_{Mg}$ and $Ti^{\cdot\cdot}_{Mg}(2H)''_{Si}$ require contaminants (and in the case of $(1H)'_{Mg}Fe^{\cdot}_{Mg}$ high oxygen fugacity) to form and thus we can establish the baseline effect of water on perfect forsterite. Second at high water concentrations which promote dislocation glide (Katayama and Karato, 2008) water is likely to outnumber the concentration of Ti and Ferric iron defects. Third we calculated the binding enthalpy (the enthalpy to remove the hydrous component from the non-hydrous component) of these two latter defects to be high- 2.2 and 5.0 eV for $(1H)'_{Mg}Fe^{\cdot}_{Mg}$ and $Ti^{\cdot\cdot}_{Mg}(2H)''_{Si}$ respectively at 5 GPa and static conditions. This means that the hydrous vacancy part of these complexes is unlikely to segregate to an forsterite dislocation (as the segregation energy of hydrous vacancies shown below is generally lower than these binding energies) and thus the entire complex would need to be segregated to the dislocation. Thus while hydrated vacancies segregate easily to dislocations as discussed below $(1H)'_{Mg}Fe^{\cdot}_{Mg}$ and $Ti^{\cdot\cdot}_{Mg}(2H)''_{Si}$ may not segregate so easily though this needs further study. For this study the only important hydrated complexes are those that will segregate to the dislocation core. Thus we shall examine $(2H)_{Mg}^{X}$ and $(4H)_{Si}^{X}$ (and V''_{Mg} and V''''_{Si}) which shall allow us to examine the dislocation mechanisms of perfect forsterite, very wet forsterite and likely also mildly wet forsterite.

Therefore we considered water existing as hydrated Mg vacancies (2H^{+}+V''_{Mg}) on the M1 or the M2 site or as hydrated Si vacancies (4H^{+}+V''''_{Si}) and calculated the relative energy for each. The relative energy of M1 and M2 hydrated vacancies is simply their energy difference, the relative energy of M1 or M2 vacancies to Si vacancies depends upon the background chemical environment. There are two major cases:

$2(2H)MgSiO_4 + 2Mg_2SiO_4 \rightarrow Mg_2(4H)O_4 + 2Mg_2Si_2O_6$ Reaction 1

$2(2H)MgSiO_4 + 4MgO \rightarrow Mg_2(4H)O_4 + 2Mg_2SiO_4$ Reaction 2

Where the first reaction represents a periloditic upper mantle where orthoenstatite is stable and reaction 2 represents a silica depleted composition. The same reaction occurs in the dry case but with dry vacancies.

These two reactions have been previously considered in detail using theoretical methods (Walker et al., 2007, Qin et al., 2018) where it is found that in enstatite $(2H)_{Mg}^{X}$ vacancies are largely favoured but in periclase $(2H)_{Mg}^{X}$ and $(4H)_{Si}^{X}$ have similar concentrations with exact conditions being important. We calculated the energies of Reaction 1 and 2 (Table 1) and found largely similar answers to these previous works with enstatite distributions shown in Figure 1 and periclase distributions in Figure S1. While $(4H)_{Si}^{X}$ is energetically favoured over $(2H)_{Mg}^{X}$ the large configurational entropy gains of pushing Reaction 1 and 2 to the right see $(2H)_{Mg}^{X}$ vacancies dominate in enstatite-buffered conditions in the lower mantle with both increased temperature or pressure favouring $(2H)_{Mg}^{X}$ and increased water concentration favouring $(4H)_{Si}^{X}$. In the case of dry vacancies Mg vacancies are overwhelmingly favoured in all conditions as both the energy and configurational terms strongly favour their formation (Table 1). In both the wet and dry case M1 Mg vacancies are significantly favoured (>0.6 eV) over M2 Mg vacancies (Table 1).

In the case of dislocation glide, however, what is important is not vacancies in a bulk crystal but vacancies that are near a dislocation which is a very different chemical environment. Simulating very large dislocations with DFT is unfeasible and so instead forcefield methods are required. The segregation of Mg vacancies in forsterite clusters was previously published in work (Skelton and Walker 2017) and here we extend this method to Si vacancies.

Figure S2 shows the segregation of dry Si vacancies and Table 2 lists the maximum energy gain of moving dry and wet vacancies to dislocation core taking into account the configurational entropy that is lost by such a movement. The energy of hydrated Silicon vacancies that is calculated by forcefields is extremely sensitive to the starting position of the hydrogen. Thus rather than generate segregation maps like we did for dry silicon instead we focused on getting the most accurate segregation energy for hydrated Si by sampling a vacancy removed from the dislocation and the 3 vacancies closest to the dislocation core and in each case trying 6 different starting hydrogen arrangements. This then allows us to calculate a segregation energy which is reported in Table 2. While the absolute energy of Si vacancies and particularly hydrated Si vacancies is likely poorly represented by forcefield calculations the relative energy of changing the stress field in which the vacancy sits should be much better formulated and thus the segregation energy of the vacancies should be reasonably accurate.

In all cases there is a strong enthalpy gain in moving a vacancy to a dislocation core with M1 vacancies gaining ~-1 eV and M2 and Si vacancies ~-2-3 eV and a strong entropy loss which can vary from +0.5-4+ eV depending on temperature and concentration but this loss is much lower for Si vacancies. As shown in Table 2 these effects combine such that Si vacancies strongly segregate to dislocation cores whereas M1 vacancies remain in the bulk and the position of M2 vacancies is condition dependant. At the dislocation cores, however, hydrated Si vacancies will be strongly favoured. Pressure, temperature and water content have little effect on this partitioning such that at all upper mantle conditions hydrated Si vacancies should dominate at dislocation cores. Figure 1 and S1 show that at decreasing temperature, decreasing SiO_2 activity and increasing water content the dominant water vacancy becomes hydrated Si vacancies at dislocation cores. Due to this we shall focus on the effects of hydrated Si vacancies on the Peierls stress but we shall also discuss the effects of any M1 or M2 vacancies that are present at dislocation cores.

Dislocation Glide in Forsterite

Elastic Constants:

Our calculated athermal elastic constants are presented in Table 3 alongside the anisotropic energy factor for the four different slip systems. These are similar to those calculated by Durinck et al. (2005). Elastic energies of a perfect crystal were used for all systems including those with vacancies as they more reliably reflect the elastic forces between individual atoms and as hydration has little effect on the elasticity of forsterite (Cline et al., 2018).

Base Forsterite

In order to consider the effect of water we first need to consider the deformation of a crystal with no vacancies. The slip planes which produce the lowest energy GSF profiles (as determined by manual search) are shown in Figure 2 - in all cases slip planes are more favourable if they avoid severing Si tetrahedra though this is not possible in the [100](001) slip system. Sample GSF and dislocation profiles can be seen in Figure 3 and 0 GPa Peierls stress and dislocation widths in Table 4 (Peierls stresses at different pressures and nonhydrated vacancies are shown in Table S2, all values from PN calculations (including edge dislocations) are shown in Tables S3-S6 and additional GSF and dislocation profiles are shown in Fig S3-S9).

The slip systems [100](010), [001](010) and [100](001) all have undissociated dislocations with similar shapes while the [001](100) slip system dissociates into two stable partial dislocations as has been seen previously (Durinck et al., 2005, Mahendran et al., 2017). Adding vacancies or pressure has negligible effects on the separation of the partial dislocations in the [001](100) system or on the shape of all dislocations only affecting their height. The one exception is the [001](010) slip system where we observed a very small dissociation that increased with pressure when dry or hydrated Si vacancies were present.

There is some controversy over the [100](010) slip system as Mahendran et al. (2017) found it has a tendency to dislocate into two partial dislocations but this was not observed by us or by Durinck et al. (2005). Dissociation of a dislocation core is typically indicative of a stable stacking fault but placing a stacking fault halfway along the dislocation line would lead to the severing of a SiO_4 tetrahedra which would create very high GSF energies as we confirmed by manually placing a stacking fault at this point. To further investigate whether the lack of dissociation in our calculations was an effect of either our system cell size or of fixing the Mg we performed calculations with a doubled [100] direction and with Mg atoms that were freely allowed to relax and in neither case was dissociation observed. Additionally the forces remaining on the atoms on either side of the glide plane were not conducive to (010) spreading. Thus the observed dissociation seen in Mahendran et al. (2017) is either an artefact of forcefield calculations or is not adequately captured in Peierls-Nabarro calculations. Regardless this dissociation was very small in Mahendran et al. (2017) and will not affect the derived Peierls stress in any large amount.

Our GSF maximums (and Peierls stresses) of 0.115/0.130/0.175/0.124 eV/ $Å^2$ for [100](010)/[001](010)/[100](001)/[001](100) slip systems are different (particularly in the [100](001) and [001](100) case) to those determined by Durinck et al. (2005) and Durinck et al. (2007) of 0.129/0.118/0.128/0.058. Both of these studies used much smaller slabs and vacuum layers to determine GSF energies but we have found that much larger slabs are needed to get accurate GSF energies. Additionally our GSF calculations contained twice as many lattice points (displacement points along the γ-line) which we also found was necessary to constrain GSF shapes accurately enough to reproduce reliable Peierls stresses. Of particular note we found that the [100](001) slip system has very high GSF energies (and thus Peierls stresses) because its slip plane passes through the centre of a SiO_4 tetrahedra which is highly unfavourable.

As shown in Table 4 screw dislocations are always harder than edge dislocations and usually by a reasonable degree (>1 GPa). As both edge and screw dislocations are required to make a dislocation loop screw dislocations thus likely control the rate of dislocation glide in forsterite. Thus we shall mostly discuss screw dislocations going forward but our edge dislocations have similar trends with both vacancies and pressure as our screw dislocations.

Figure 4 shows a plot of the Peierls stresses of the screw dislocations as a function of pressure. Slips with [100] cores tend to harden with pressure while slips with [001] cores have little variation or soften with pressure. Our results do not match with experimental deformation studies which show that at 0 GPa [100](010) slip is dominant converting to [001](010) slip at ~6.75-8 GPa (Raterron et al., 2009, Raterron et al., 2007, Raterron et al., 2011, Raterron et al., 2012, Ohuchi et al., 2012). This discrepancy is due to the non-planar nature of the [001] screw dislocation (Mahendran et al., 2017, Carrez et al., 2008). Using interatomic forcefields on large systems and the application of direct shear to the system Mahendran et al. (2017) found that in order to glide [001] screw dislocations must first convert to a planar core. The results of Mahendran et al. (2017) are shown in Table 4 and compared to our results. There are two significant differences between our computational regime and that of Mahendran et al. (2017)- one in computational approach (DFT vs forcefield) and one in method (PN vs directly applied stress). Our approach should determine the resistance to flow of a planar core more accurately but it does not consider the rate of conversion of non-planar cores to planar cores and so we need to apply a correction to our [001] screw systems to account for this locking-unlocking rate. Neither pressure nor vacancies cause a significant change in the shape of [001] dislocations (Figures S4 and S6) and thus do not change their core structure. This means that neither of these variables should affect the locking-unlocking rate and a fixed correction which is invariant with pressure or vacancies can be applied. This correction was then determined by simply taking the difference between our predictions of [001](100) and [001](100) screw stresses at 0 GPa and those of Mahendran et al. (2017) and applying this fixed number as a correction to all screw stresses in the relevant slip system regardless of pressure or vacancy presence. These values shall then be referred to as the “corrected” values.

While this is a crude and artificial method it is conceptually the most straightforward and it produces a [100](010) to [001](010) crossover of 7.66 GPa which is inside the experimental range. From this starting point our results robustly predict the effect of vacancies and pressure on planar glide and so they can accurately predict the effect of modifications to the crystal on overall Peierls stresses. This method would only breakdown if vacancies or pressure have a strong effect on the unlocking-locking rate of the [001] screw dislocation but this is unlikely.

The Effect of Vacancies on Peierls Stresses

Adding vacancies has a large effect on the Peierls stress of all slip systems and can change the favoured slip system.

Firstly we shall consider the most likely vacancies at the dislocation cores- hydrated Si vacancies. As shown in Figure 5 with hydrated Si vacancies the [001](100) slip system is activated such that it is the weakest slip system at all pressures examined (0-10 GPa). Both the [001](100) and [100](001) slip systems are made easier (Fig S10) whereas the [100](010) and [001](010) slip systems are less affected. This is because in the former two systems the slip planes cuts through the centre or the corner of a SiO_4 tetrahedral and so replacing the Si with a vacancy reduces the barrier to distorting/breaking the tetrahedron. The difference between hydrated and non-hydrated vacancies (shown in Fig S10) is small for the most stabilised [001](100) system but is on the same order of adding a vacancy for the other 3 slip systems. Dry Si vacancies are exceedingly rare (Table 1), however, and so only wet Si vacancies need to be considered.

The next most likely vacancies are M2 vacancies. These cause a very large decrease in Peierls stress in the [100](010), [001](010), the dry [100](001) and the wet [001](100) systems (Figure S11-S12). [100](010) slip is easiest at all pressures but the barrier to planar glide of the [001](010) slip system approaches 0 when M2 vacancies are present and its unfavourability is entirely due to its assigned locking-unlocking rate. For those systems with

(010) slip planes the large reduction in Peierls stress with M2 vacancies is due to the slip planes containing an M2 atom and removing this atom removes a barrier to slip which occurs similarly in both wet and dry cases. In the other two slip systems there are complex interplays between charge, hydrogen positioning and slip plane barriers.

M1 vacancies are unlikely to be present at dislocations but we shall still consider their effects (Figure S13 and S14). M1 vacancies produce large stabilisations of the [100](001) slip system but not enough to make it favourable. Of the other slip systems the [100](010) slip system is stabilised the most and so like with M2 vacancies this slip system becomes favoured throughout upper mantle pressures. As with M2 vacancies the effect of hydrating the vacancy is small compared to the act of simply introducing the vacancy for slip systems in the (010) plane and so wet and dry M1 vacancies operate similarly.

Fabric Development in the presence of Vacancies

To illustrate these cases we then predicted the resulting fabric of our forsterite in various conditions using the D-Rex code. Using our raw uncorrected data in all tested cases a clear B fabric develops (Figure S15). This is expected as the Peierls stress of the [001](010) slip system is the lowest when not considering the effects of [001] non-planarity. With our corrected data (Figure 6 and 7) we see that water can make clear modifications to the texture. In the absence of vacancies, increasing the pressure switches the developed fabric from A to B. With hydrated Si vacancies (non-hydrated vacancies are shown in Figure S16) an A texture with some weak C texture is seen at 0 GPa that develops by 10 GPa into a mixture of A, B and C textures. This effect happens because while the [001](100) and [001](010) slip systems have Peierls stresses that mildly harden/weaken with pressure (Figure 4) the [100](010) slip system hardens significantly with pressure and thus the A fabric weakens with pressure. This indicates that some pressure, as well as water, is needed to form C fabrics in forsterite. With hydrated M1 and M2 vacancies (Figure 7) a strong A fabric is observed throughout our pressure range- as expected from their slip system activities- and so only Si vacancies can induce strong texture changes in forsterite.

Discussion:

Our main overall conclusion is that water induces a C fabric and somewhat a B fabric in forsterite solely through modifying the relative Peierls stress of different slip systems. This effect increases with pressure because the [100](010) slip system hardens with pressure. This mechanism operates through the segregation of hydrous Si vacancies to dislocation cores. If Mg vacancies were present A fabrics would be promoted by water but this is inconsistent with both experiment and the energetics of vacancy segregation. E fabrics cannot be produced under dislocation glide conditions because of the very high Peierls stress of [100](001) slip under all conditions. Using this information we can attempt to elucidate some of the observed literature results.

In dry (<40 ppm) forsterite a fabric transition from A to B (or B-like with some C components) occurs with pressure. This has been observed with EBSD measurements after deformation (Jung et al., 2009, Ohuchi et al., 2011, Bollinger et al., 2016) and via direct monitoring of the strength of different slip systems (Raterron et al., 2009, Raterron et al., 2007, Raterron et al., 2011, Raterron et al., 2012). The pressure of this transition is varied from ~3 GPa (Jung et al., 2009) to 6-8 GPa (Ohuchi et al., 2011, Raterron et al., 2007, Raterron et al., 2011). We find that this transition can be easily explained by the different pressure derivatives of the slip systems as has also been seen by Raterron et al. (2011). This transition is entirely controlled by the locking-unlocking rate of the [001] screw dislocation core as a planar [001] screw dislocation core always glides easier in the (010) plane than the [100] screw core. This rate (which we cannot determine with these methods) is highly likely to be controlled by stress. A stress-induced decrease in the locking-unlocking rate would explain the stress induced transition to B fabrics that has been previously observed (Jung and Karato, 2001, Jung et al., 2006, Katayama and Karato, 2006) at ~300 MPa. Additionally in Ohuchi et al. (2011) it was observed that B fabrics (as opposed to mixed B-like fabrics) formed with increasing clarity at lower temperatures but these lower temperature runs also had higher stresses which would aid B fabric formation under such a system.

In wet forsterite a variety of effects have been seen. Firstly at low stresses <~200 MPa and pressures ~2 GPa an A to E transition was observed for moderate amounts of water (< 800 ppm H/Si) and an A to C or E to C transition for larger amounts of water (Jung et al., 2006, Katayama et al., 2004, Jung and Karato, 2001). At higher pressures (>10 GPa) a C fabric is developed with a very wide range of water (50-29000 ppm H/Si) (Couvy et al., 2004, Ohuchi and Irifune, 2014). Our results predict that water will promote C (and somewhat B) fabrics simply by hydrous modification of relative Peierls stresses but that some additional pressure is required to resolve the fabrics which explains the fact that C fabrics are more commonly observed at high pressures in experiments.

The production of E fabrics with moderate water contents is more vexing. Our results find that under all pressure and vacancy conditions the [100](001) slip system has a considerably higher Peierls stress than other slip systems. There is no obvious modification that will lower the Peierls stress of this slip system as it will always sever a SiO_4 tetrahedron which is energetically unfavourable. Experimentally Tielke et al. (2016) found the Peierls stress of [100](001) slip to be ~3 times larger than [001](100) in the glide controlled region which is similar to our ratios of 1.6-2.2 in the dry regime and 2.2-2.7 in the wet regime. Thus while the production of A, B and C fabrics can be explained through a Peierls mechanism the production of E fabrics at moderate water contents likely indicates a different deformation mechanism is dominant. There is some evidence that E fabrics would be promoted in a diffusion regime as Tielke et al. (2016) found that [100](001) slip is easier than [001](100) slip in a climb-controlled regime and Tielke et al. (2017) found that hydrated olivine primarily has [100] slips in climb-controlled wet olivine.

As water concentration increases the rate of dislocation creep should also increase relative to that of diffusion creep. This is because water increases the olivine grain size (Jung and Karato, 2001) and lowers the stress barrier to convert from diffusion to dislocation creep (Katayama and Karato, 2008). Experimentally it has been seen that water can convert curved dislocation lines to straight ones (Jung et al., 2006) which also shows an increasing preference for dislocation creep in wet systems. Thus the preference of E fabrics at low water contents is indicative of other deformation mechanisms operating which are supressed with higher water contents leading to the production of C fabrics under a typical dislocation glide regime. As pressure increases, dislocation creep is also favoured (Fei et al., 2016) which could explain why E fabrics have not been observed at higher pressures as dislocation creep is always the dominant deformation mechanism at high pressures regardless of water content.

Outside of the production of E fabrics, experimentally the effect of water on fabric development has no concentration effect as at high pressure C fabrics are formed from 50-20,000 ppm (Ohuchi and Irifune, 2014). Our wet model demonstrates a saturated end-point where the dislocation glide barrier is controlled by a wet vacancy. To consider the effects of water concentration we thus need to know the relative concentration of dislocations vs the relative concentration of water. The dislocation density can be approximated as $\rho = b\sigma^m$ where b is $10^{9.04}$, m is 1.41, σ is the stress (in MPa) and ρ is dislocation density (in m^{-2}) (Karato and Jung, 2003) such that at a typical lower mantle stress (80 MPa) the dislocation density is 5.3E-11 m^{-2}. The equivalent water concentration (enough water to saturate every dislocation) is ~200 ppm (H/Si) for dislocations with (010) slip and ~300 ppm for those with (100) slip. The required concentration to induce a fabric is likely much lower than this as ~10% of the dislocations carries 95% of the strain in forsterite (Boioli et al., 2015a) which would move this transition to ~60-90 ppm. Beyond this saturation point the water will overwhelmingly reside in the bulk and should have no effect on the fabric transition and thus for any reasonably wet (>~90 ppm) sample water should simply enable C fabrics with no concentration effects. Under more high stress conditions (450 MPa) we find that that 10% saturation would be achieved at a water concentration of 200-300 ppm and thus stress has a small effect on the saturation limit of dislocations.

A different set of relations has been seen with wet forsterite at high stress. At low pressures (~2 GPa) stress above ~300 MPa has been seen to convert A/E/C fabrics to B fabrics (Katayama and Karato, 2008, Jung et al., 2006, Jung and Karato, 2001, Katayama and Karato, 2006), and at high pressures (7.2-11.1 GPa, 400 MPa stress) (Ohuchi and Irifune, 2013) to convert C fabrics to B and then to A fabrics with increasing amounts of water though there is some debate about this barrier as B fabrics have been produced in wet forsterite at ~2.1-5.2 GPa and below <300 MPa stresses (Ohuchi et al., 2012). As temperature decreases the required stress to convert to B fabrics will also decrease (Katayama and Karato, 2006)- at a typical lower mantle stress of 80 MPa C fabrics will be produced in favour of B at temperatures greater than 1173 K but at a high stress of 450 MPa this temperature rises to ~1600 K. As discussed above the conversion of A or C fabrics to B fabrics is likely related to the unlocking-locking rate of the [001] screw dislocation. In both the dry and the wet case planar glide of the [001](010) slip system is the easiest slip system and so increasing the rate at which this screw dislocation becomes planar (if the locking-unlocking rate decreases with stress) will improve the formation of B fabrics at all water concentrations. The formation of A fabrics with large amounts of water and stress (Ohuchi and Irifune, 2013) has a less obvious source but is perhaps related to the fact that Mg vacancies (which will be present with such large amounts of water) promote A fabrics.

There are two other common stress mechanisms but they are unlikely to cause the formation of B fabrics. The most obvious effect of stress on dislocation creep is an increase in the number of dislocations with dislocation density increasing from 5.3E+11 m^{-2} at 80 MPa to 6.0E+12 m^{-2} at 450 MPa (Karato and Jung, 2003). The variation in these values is much lower than the variation of water contents across experimental ranges which does not induce B fabrics and so this should not be a factor in B fabric formation. The other possibility is that stress has a varying effects on the ease of glide of different slip systems. This will not be a factor if the stress exponents are the same for all slip systems which is true for dry forsterite (Durham et al., 1977) but is possibly not true for wet forsterite. We find that water does not have a large effect on the shape of dislocations and thus it is unlikely to affect the stress exponent of the dislocation and thus we expect wet forsterite to have the same stress exponent for all slip systems.

We have considered only high temperature results (>1373 K) so far. At low temperatures forsterite polycrystalline powders show weak CPO textures with both [100] and [001] dislocations that glide on both standard and non-standard glide planes (Demouchy et al., 2014) whereas single crystal experiments show [001] dislocations that glide on (010), (100) and (110) planes as well as (001)[010] slip (Demouchy et al., 2013, Durham et al., 1977, Phakey et al., 1971, Demouchy et al., 2009, Evans and Goetze, 1979, Raleigh, 1968). Polycrystalline powders also show a rapid conversion from low temperature to high temperature dislocation glide patterns at ~1373 K (Demouchy et al., 2013, Bai et al., 1991, Raleigh, 1968). While the presence of [001] slip at low temperatures can be tied to a reduction in the stress barrier to forming B fabrics (Katayama and Karato, 2006), the complex nature of the observed slips at low temperature indicates that multiple deformation effects are occurring (Bai et al., 1991) and thus more work would be needed to evaluate these systems which would include considering diffusional effects and calculating the slip of non-standard glide planes.

A final consideration is the effect of water and pressure on the activation volume of forsterite which is important for calculating its deformation as a function of depth. In dry olivine the activation volume has been observed to decrease from 15±3 to 0±1.2 cm/mol^3 by increasing the pressure (Raterron et al., 2011) while Kaboli et al. (2017) also found a decrease from ~15 to ~4 cm/mol^3 though without a strong control on water content. We find that the pressure dependence on the dry Peierls stress decreases by ~3 times and it switches sign by converting from [100](010) to [001](010) slip and so a large drop in activation volume can be explained by simply the pressure dependence of the Peierls stress for the two (010) slip systems. While early studies found that the activation volume of wet olivine was similar to dry olivine eg. (Karato and Wu, 1993) a Markov-chain reanalysis of previous published data (Korenaga and Karato, 2008) found that dry olivine has an activation volume of 13±8 and wet olivine 4±3 such that a significant decrease in activation volume with hydration is likely. The large scatter of activation volumes of nominally dry olivine is likely also an indicator that activation volume is sensitive to water fugacity (Ohuchi et al., 2017). We find that the pressure dependence of the Peierls stress decreases by ~5 times (depending on pressure) (Table 5) on going from dry [100](010) to wet [001](100) slip. This is important as it shows that water can strongly reduce the activation volume of forsterite simply by modifying the Peierls stress alone without invoking other activation mechanisms.

Conclusions:

In conclusion the introduction of hydrated vacancies into forsterite promotes C fabrics through the formation of Si vacancies enabling [001](100) slip. This transition should be insensitive to water content but increases with pressure. The activation volume of deformation is sharply decreased with hydration. The production of E fabrics cannot occur in a purely Peierls-based creep system and the production of B fabrics under high stress likely involves some additional mechanism that we are not considering such as a change in the locking-unlocking rate.

BAI, Q., MACKWELL, S. J. & KOHLSTEDT, D. L. 1991. HIGH-TEMPERATURE CREEP OF OLIVINE SINGLE-CRYSTALS .1. MECHANICAL RESULTS FOR BUFFERED SAMPLES. *Journal of Geophysical Research-Solid Earth and Planets,* 96**,** 2441-2463.

BOIOLI, F., CARREZ, P., CORDIER, P., DEVINCRE, B. & MARQUILLE, M. 2015a. Modeling the creep properties of olivine by 2.5-dimensional dislocation dynamics simulations. *Physical Review B,* 92.

BOIOLI, F., TOMMASI, A., CORDIER, P., DEMOUCHY, S. & MUSSI, A. 2015b. Low steady-state stresses in the cold lithospheric mantle inferred from dislocation dynamics models of dislocation creep in olivine. *Earth and Planetary Science Letters,* 432**,** 232-242.

BOLLINGER, C., RATERRON, P., CASTELNAU, O., DETREZ, F. & MERKEL, S. 2016. Textures in deforming forsterite aggregates up to 8 GPa and 1673 K. *Physics and Chemistry of Minerals,* 43**,** 409-417.

BRODHOLT, J. P. & REFSON, K. 2000. An ab initio study of hydrogen in forsterite and a possible mechanism for hydrolytic weakening. *Journal of Geophysical Research-Solid Earth,* 105**,** 18977-18982.

BULATOV, V. V. & KAXIRAS, E. 1997. Semidiscrete variational Peierls framework for dislocation core properties. *Physical Review Letters,* 78**,** 4221-4224.

CARREZ, P., WALKER, A. M., METSUE, A. & CORDIER, P. 2008. Evidence from numerical modelling for 3D spreading of 001 screw dislocations in Mg(2)SiO(4) forsterite. *Philosophical Magazine,* 88**,** 2477-2485.

CLARK, S. J., SEGALL, M. D., PICKARD, C. J., HASNIP, P. J., PROBERT, M. J., REFSON, K. & PAYNE, M. C. 2005. First principles methods using CASTEP. *Zeitschrift fuer Kristallographie,* 220**,** 567-570.

CLINE, C. J., FAUL, U. H., DAVID, E. C., BERRY, A. J. & JACKSON, I. 2018. Redox-influenced seismic properties of uppermantle olivine. *Nature,* 555**,** 355-+.

COUVY, H., FROST, D. J., HEIDELBACH, F., NYILAS, K., UNGAR, T., MACKWELL, S. & CORDIER, P. 2004. Shear deformation experiments of forsterite at 11GPa-1400 degrees C in the multianvil apparatus. *European Journal of Mineralogy,* 16**,** 877-889.

DEMOUCHY, S., MUSSI, A., BAROU, F., TOMMASI, A. & CORDIER, P. 2014. Viscoplasticity of polycrystalline olivine experimentally deformed at high pressure and 900 degrees C. *Tectonophysics,* 623**,** 123-135.

DEMOUCHY, S., SCHNEIDER, S. E., MACKWELL, S. J., ZIMMERMAN, M. E. & KOHLSTEDT, D. L. 2009. Experimental deformation of olivine single crystals at lithospheric temperatures. *Geophysical Research Letters,* 36.

DEMOUCHY, S., TOMMASI, A., BALLARAN, T. B. & CORDIER, P. 2013. Low strength of Earth's uppermost mantle inferred from tri-axial deformation experiments on dry olivine crystals. *Physics of the Earth and Planetary Interiors,* 220**,** 37-49.

DURHAM, W. B., GOETZE, C. & BLAKE, B. 1977. PLASTIC-FLOW OF ORIENTED SINGLE-CRYSTALS OF OLIVINE .2. OBSERVATIONS AND INTERPRETATIONS OF DISLOCATION-STRUCTURES. *Journal of Geophysical Research,* 82**,** 5755-5770.

DURINCK, J., DEVINCRE, B., KUBIN, L. & CORDIER, P. 2007. Modeling the plastic deformation of olivine by dislocation dynamics simulations. *American Mineralogist,* 92**,** 1346-1357.

DURINCK, J., LEGRIS, A. & CORDIER, P. 2005. Pressure sensitivity of olivine slip systems: first-principle calculations of generalised stacking faults. *Physics and Chemistry of Minerals,* 32**,** 646-654.

EVANS, B. & GOETZE, C. 1979. TEMPERATURE-VARIATION OF HARDNESS OF OLIVINE AND ITS IMPLICATION FOR POLYCRYSTALLINE YIELD STRESS. *Journal of Geophysical Research,* 84**,** 5505-5524.

FAUL, U. H., GERALD, J. D. F., FARLA, R. J. M., AHLEFELDT, R. & JACKSON, I. 2011. Dislocation creep of fine-grained olivine. *Journal of Geophysical Research-Solid Earth,* 116.

FEI, H., KOIZUMI, S., SAKAMOTO, N., HASHIGUCHI, M., YURIMOTO, H., MARQUARDT, K., MIYAJIMA, N., YAMAZAKI, D. & KATSURA, T. 2016. New constraints on upper mantle creep mechanism inferred from silicon grain-boundary diffusion rates. *Earth and Planetary Science Letters,* 433**,** 350-359.

GALE, J. D. 1997. GULP - a computer program for the symmetry adapted simulation of solids. *JCS Faraday Trans,* 93**,** 629-637.

HIRSCHMANN, M. M. 2006. Water, melting, and the deep Earth H(2)O cycle. *Annual Review of Earth and Planetary Sciences.*

JUNG, H. 2017. Crystal preferred orientations of olivine, orthopyroxene, serpentine, chlorite, and amphibole, and implications for seismic anisotropy in subduction zones: a review. *Geosciences Journal,* 21**,** 985-1011.

JUNG, H. & KARATO, S. 2001. Water-induced fabric transitions in olivine. *Science,* 293**,** 1460-1463.

JUNG, H., KATAYAMA, I., JIANG, Z., HIRAGA, T. & KARATO, S. 2006. Effect of water and stress on the lattice-preferred orientation of olivine. *Tectonophysics,* 421**,** 1-22.

JUNG, H., MO, W. & GREEN, H. W. 2009. Upper mantle seismic anisotropy resulting from pressure-induced slip transition in olivine. *Nature Geoscience,* 2**,** 73-77.

KABOLI, S., BURNLEY, P. C., XIA, G. & GREEN, H. W. 2017. Pressure Dependence of Creep in Forsterite Olivine: Comparison of Measurements From the D-DIA and Griggs Apparatus. *Geophysical Research Letters,* 44**,** 10939-10947.

KAMINSKI, E. 2002. The influence of water on the development of lattice preferred orientation in olivine aggregates. *Geophysical Research Letters,* 29.

KAMINSKI, E., RIBE, N. M. & BROWAEYS, J. 2004. D-Rex, a program for calculation of seismic anisotropy due to crystal lattice preferred orientation in the convective upper mantle. *Geophysical Journal International,* 158**,** 744-752.

KARATO, S.-I., JUNG, H., KATAYAMA, I. & SKEMER, P. 2008a. Geodynamic significance of seismic anisotropy of the upper mantle: New insights from laboratory studies. *Annual Review of Earth and Planetary Sciences.*

KARATO, S. 2011. Water distribution across the mantle transition zone and its implications for global material circulation. *Earth and Planetary Science Letters,* 301**,** 413-423.

KARATO, S., JUNG, H., KATAYAMA, I. & SKEMER, P. 2008b. Geodynamic significance of seismic anisotropy of the upper mantle: New insights from laboratory studies. *Annual Review of Earth and Planetary Sciences.*

KARATO, S. & WU, P. 1993. RHEOLOGY OF THE UPPER MANTLE - A SYNTHESIS. *Science,* 260**,** 771-778.

KARATO, S. I. & JUNG, H. 2003. Effects of pressure on high-temperature dislocation creep in olivine. *Philosophical Magazine,* 83**,** 401-414.

KATAYAMA, I., JUNG, H. & KARATO, S. I. 2004. New type of olivine fabric from deformation experiments at modest water content and low stress. *Geology,* 32**,** 1045-1048.

KATAYAMA, I. & KARATO, S. 2006. Effect of temperature on the B- to C-type olivine fabric transition and implication for flow pattern in subduction zones. *Physics of the Earth and Planetary Interiors,* 157**,** 33-45.

KATAYAMA, I. & KARATO, S. I. 2008. Low-temperature, high-stress deformation of olivine under water-saturated conditions. *Physics of the Earth and Planetary Interiors,* 168**,** 125-133.

KAWAZOE, T., KARATO, S.-I., OTSUKA, K., JING, Z. & MOOKHERJEE, M. 2009. Shear deformation of dry polycrystalline olivine under deep upper mantle conditions using a rotational Drickamer apparatus (RDA). *Physics of the Earth and Planetary Interiors,* 174**,** 128-137.

KNELLER, E. A., VAN KEKEN, P. E., KARATO, S. & PARK, J. 2005. B-type olivine fabric in the mantle wedge: Insights from high-resolution non-Newtonian subduction zone models. *Earth and Planetary Science Letters,* 237**,** 781-797.

KNELLER, E. A., VAN KEKEN, P. E., KATAYAMA, I. & KARATO, S. 2007. Stress, strain, and B-type olivine fabric in the fore-arc mantle: Sensitivity tests using high-resolution steady-state subduction zone models. *Journal of Geophysical Research,* 112**,** B04406.

KORENAGA, J. & KARATO, S.-I. 2008. A new analysis of experimental data on olivine rheology. *Journal of Geophysical Research-Solid Earth,* 113.

LE LOSQ, C., JOLLANDS, M. C., TOLLAN, P. M. E., HAWKINS, R. & O'NEILL, H. S. C. 2019. Point defect populations of forsterite revealed by two-stage metastable hydroxylation experiments. *Contributions to Mineralogy and Petrology,* 174.

LESLIE, M. & GILLAN, M. J. 1985. THE ENERGY AND ELASTIC DIPOLE TENSOR OF DEFECTS IN IONIC-CRYSTALS CALCULATED BY THE SUPERCELL METHOD. *Journal of Physics C-Solid State Physics,* 18**,** 973-982.

LEWIS, G. V. & CATLOW, C. R. A. 1985. POTENTIAL MODELS FOR IONIC OXIDES. *Journal of Physics C-Solid State Physics,* 18**,** 1149-1161.

MACKWELL, S. J., KOHLSTEDT, D. L. & PATERSON, M. S. 1985. THE ROLE OF WATER IN THE DEFORMATION OF OLIVINE SINGLE-CRYSTALS. *Journal of Geophysical Research-Solid Earth and Planets,* 90**,** 1319-1333.

MAHENDRAN, S., CARREZ, P., GROH, S. & CORDIER, P. 2017. Dislocation modelling in Mg2SiO4 forsterite: an atomic-scale study based on the THB1 potential. *Modelling and Simulation in Materials Science and Engineering,* 25**,** 18.

MICHIBAYASHI, K., MAINPRICE, D., FUJII, A., UEHARA, S., SHINKAI, Y., KONDO, Y., OHARA, Y., ISHII, T., FRYER, P., BLOOMER, S. H., ISHIWATARI, A., HAWKINS, J. W. & JI, S. C. 2016. Natural olivine crystal-fabrics in the western Pacific convergence region: A new method to identify fabric type. *Earth and Planetary Science Letters,* 443**,** 70-80.

NABARRO, F. R. N. 1947. DISLOCATIONS IN A SIMPLE CUBIC LATTICE. *Proceedings of the Physical Society of London,* 59**,** 256-272.

NISHIHARA, Y., OHUCHI, T., KAWAZOE, T., SPENGLER, D., TASAKA, M., KIKEGAWA, T., SUZUKI, A. & OHTANI, E. 2014. Rheology of fine-grained forsterite aggregate at deep upper mantle conditions. *Journal of Geophysical Research-Solid Earth,* 119**,** 253-273.

OHUCHI, T. & IRIFUNE, T. 2013. Development of A-type olivine fabric in water-rich deep upper mantle. *Earth and Planetary Science Letters,* 362**,** 20-30.

OHUCHI, T. & IRIFUNE, T. 2014. Crystallographic preferred orientation of olivine in the Earth's deep upper mantle. *Physics of the Earth and Planetary Interiors,* 228**,** 220-231.

OHUCHI, T., KARATO, S.-I. & FUJINO, K. 2011. Strength of single-crystal orthopyroxene under lithospheric conditions. *Contributions to Mineralogy and Petrology,* 161**,** 961-975.

OHUCHI, T., KAWAZOE, T., HIGO, Y. & SUZUKI, A. 2017. Flow behavior and microstructures of hydrous olivine aggregates at upper mantle pressures and temperatures. *Contributions to Mineralogy and Petrology,* 172**,** 26.

OHUCHI, T., KAWAZOE, T., NISHIHARA, Y. & IRIFUNE, T. 2012. Change of olivine a-axis alignment induced by water: Origin of seismic anisotropy in subduction zones. *Earth and Planetary Science Letters,* 317**,** 111-119.

PHAKEY, P. P., DOLLINGE.G & CHRISTIE, J. M. 1971. TRANSMISSION ELECTRON MICROSCOPY OF EXPERIMENTALLY DEFORMED OLIVINE CRYSTALS. *Transactions-American Geophysical Union,* 52**,** 919-&.

QIN, T., WENTZCOVITCH, R. M., UMEMOTO, K., HIRSCHMANN, M. M. & KOHLSTEDT, D. L. 2018. Ab initio study of water speciation in forsterite: Importance of the entropic effect. *American Mineralogist,* 103**,** 692-699.

RALEIGH, C. B. 1968. MECHANISMS OF PLASTIC DEFORMATION OF OLIVINE. *Journal of Geophysical Research,* 73**,** 5391-&.

RATERRON, P., AMIGUET, E., CHEN, J. H., LI, L. & CORDIER, P. 2009. Experimental deformation of olivine single crystals at mantle pressures and temperatures. *Physics of the Earth and Planetary Interiors,* 172**,** 74-83.

RATERRON, P., CHEN, J., LI, L., WEIDNER, D. & CORDIER, P. 2007. Pressure-induced slip-system transition in forsterite: Single-crystal rheological properties at mantle pressure and temperature. *American Mineralogist,* 92**,** 1436-1445.

RATERRON, P., CHEN, J. H., GEENEN, T. & GIRARD, J. 2011. Pressure effect on forsterite dislocation slip systems: Implications for upper-mantle LPO and low viscosity zone. *Physics of the Earth and Planetary Interiors,* 188**,** 26-36.

RATERRON, P., GIRARD, J. & CHEN, J. H. 2012. Activities of olivine slip systems in the upper mantle. *Physics of the Earth and Planetary Interiors,* 200**,** 105-112.

SCHRODER, K. P., SAUER, J., LESLIE, M., CATLOW, C. R. A. & THOMAS, J. M. 1992. BRIDGING HYDROXYL-GROUPS IN ZEOLITIC CATALYSTS - A COMPUTER-SIMULATION OF THEIR STRUCTURE, VIBRATIONAL PROPERTIES AND ACIDITY IN PROTONATED FAUJASITES (H-Y ZEOLITES). *Chemical Physics Letters,* 188**,** 320-325.

SKELTON, R. & WALKER, A. M. 2017. Peierls-Nabarro modeling of dislocations in UO_2. *Journal of Nuclear Materials,* 495**,** 202-210.

TIELKE, J. A., ZIMMERMAN, M. E. & KOHLSTEDT, D. L. 2016. Direct shear of olivine single crystals. *Earth and Planetary Science Letters,* 455**,** 140-148.

TIELKE, J. A., ZIMMERMAN, M. E. & KOHLSTEDT, D. L. 2017. Hydrolytic weakening in olivine single crystals. *Journal of Geophysical Research-Solid Earth,* 122**,** 3465-3479.

TOLLAN, P. M. E., O'NEILL, H. S. C. & HERMANN, J. 2018. The role of trace elements in controlling H incorporation in San Carlos olivine. *Contributions to Mineralogy and Petrology,* 173.

WALKER, A. M., HERMANN, J., BERRY, A. J. & O'NEILL, H. S. 2007. Three water sites in upper mantle olivine and the role of titanium in the water weakening mechanism. *Journal of Geophysical Research-Solid Earth,* 112**,** 12.

WANG, D., MOOKHERJEE, M., XU, Y. & KARATO, S.-I. 2006. The effect of water on the electrical conductivity of olivine. *Nature,* 443**,** 977-980.

WANG, Q. 2016. Homologous temperature of olivine: Implications for creep of the upper mantle and fabric transitions in olivine. *Science China-Earth Sciences,* 59**,** 1138-1156.

WRIGHT, K. & CATLOW, C. R. A. 1994. A computer simulation study of (OH) defects in olivine. *Physics and Chemistry of Minerals,* 20**,** 515-518.

YOSHINO, T., MATSUZAKI, T., YAMASHITA, S. & KATSURA, T. 2006. Hydrous olivine unable to account for conductivity anomaly at the top of the asthenosphere. *Nature,* 443**,** 973-976.

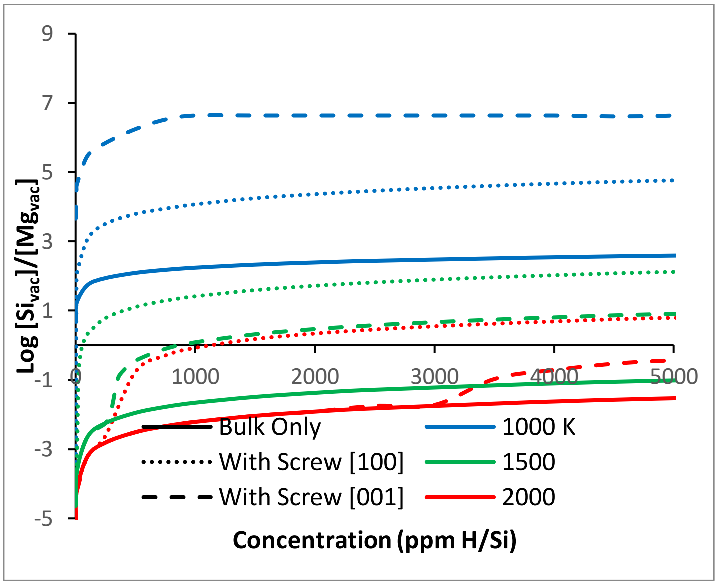

Figure 1: Ratio of the concentration of wet Si vacancies compared to wet Mg vacancies (M1+M2) for a varying water content at 5 GPa, in the presence of orthopyroxene (Reaction 1) and at different temperatures (1000, 1500 and 2000 K blue green and red respectively). Three different cases are shown- one with a pure bulk system (solid lines) and two with either a [100] screw dislocation core (dotted lines) or a [001] screw dislocation core (dashed lines) that vacancies can partition to. The systems with dislocation cores at some concentration develop excess Si vacancies- these Si vacancies are the one that partition to the dislocation core.

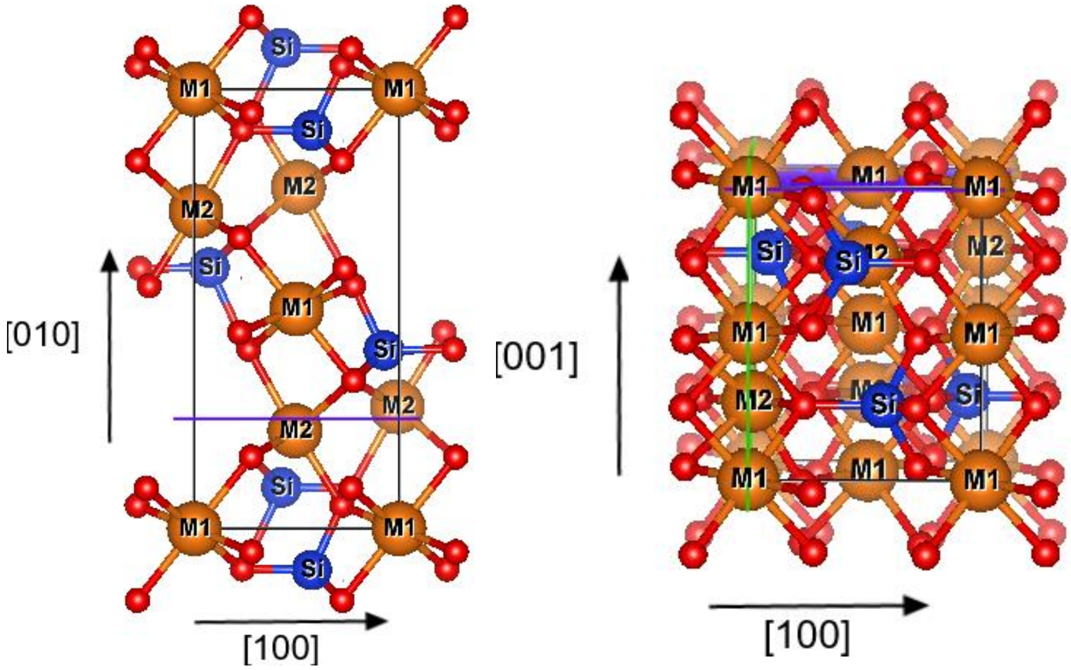

Fig 2: Illustration of the unit cell of forsterite with the energetically lowest slip planes for the [100](010) and [001](010) fabrics marked on the left in blue and for the [100](001) and [001](100) fabrics marked on the right in green and blue respectively.

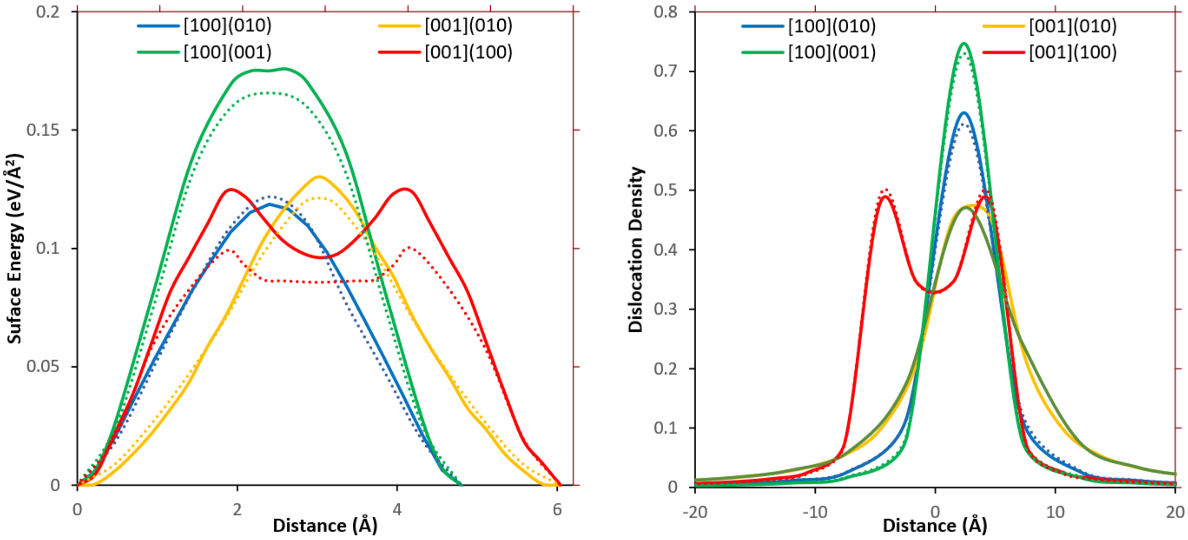

Figure 3: A) Sample γ-lines and B) sample screw dislocation density plots for forsterite containining no vacancies (solid line) and a hydrated Si vacancy (dotted line) for the [100](010), [001](010), [100](001) and [001](100) slip systems at 0 GPa. The effect of pressure and other vacancies on the GSF profiles can be seen in Fig S3,S4, S5 and S6 whereas the equivalent edge dislocation density plots can be seen in Fig S7 and the dislocation density plots for M1 and M2 vacancies in Fig S8 and Fig S9. Pressure has little effect on the shape of either plot.

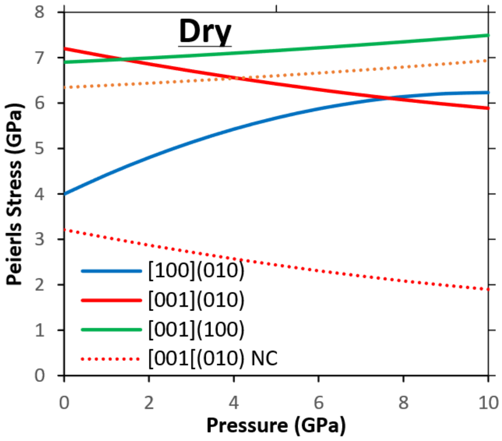

Figure 4: Plot of the Peierls stress of the screw dislocations as a function of pressure for 4 slip systems. Two lines are shown for the slip systems with [001] Burgers vector- the dotted line is our calculated value whereas the solid line is our corrected value as discussed in the text.

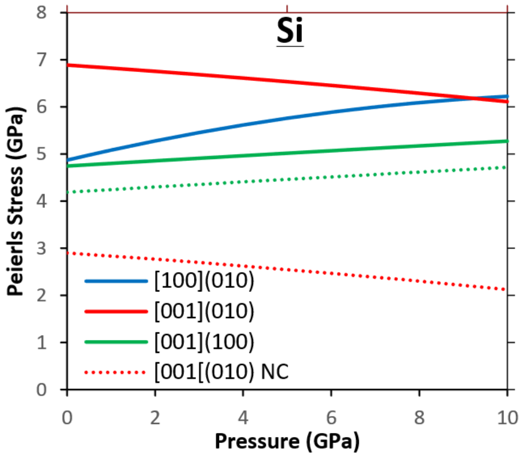

Figure 5: As Figure 3 but with a hydrated Silicon vacancy near the slip plane.

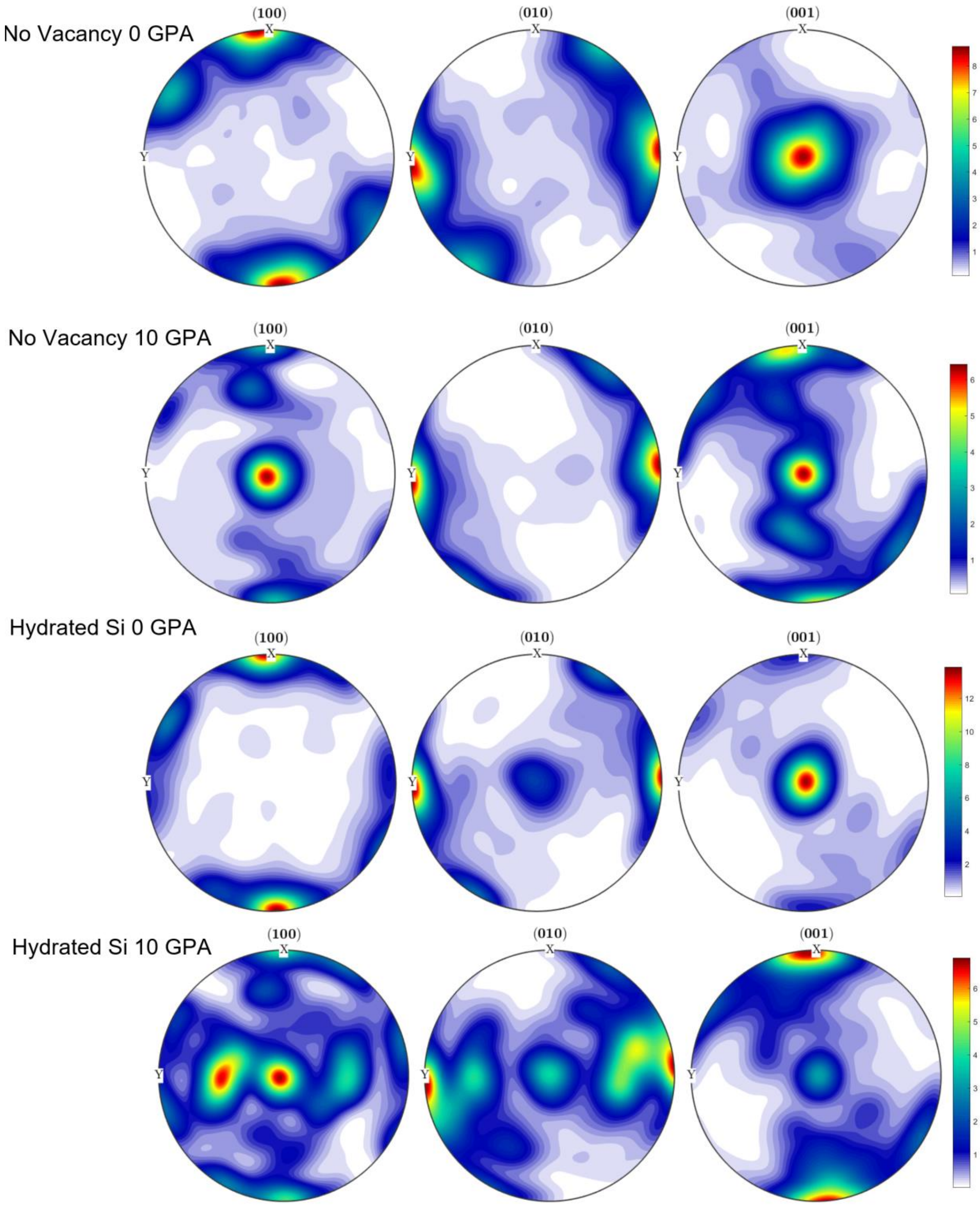

Figure 6: D-Rex simulations of forsterite textures with and without a hydrated Si vacancy near the slip plane and at 0 and 10 GPa. Corrected Peierls stresses are used for the CRRS. In all our D-Rex projections shear is in x direction and xy is the shear plane.

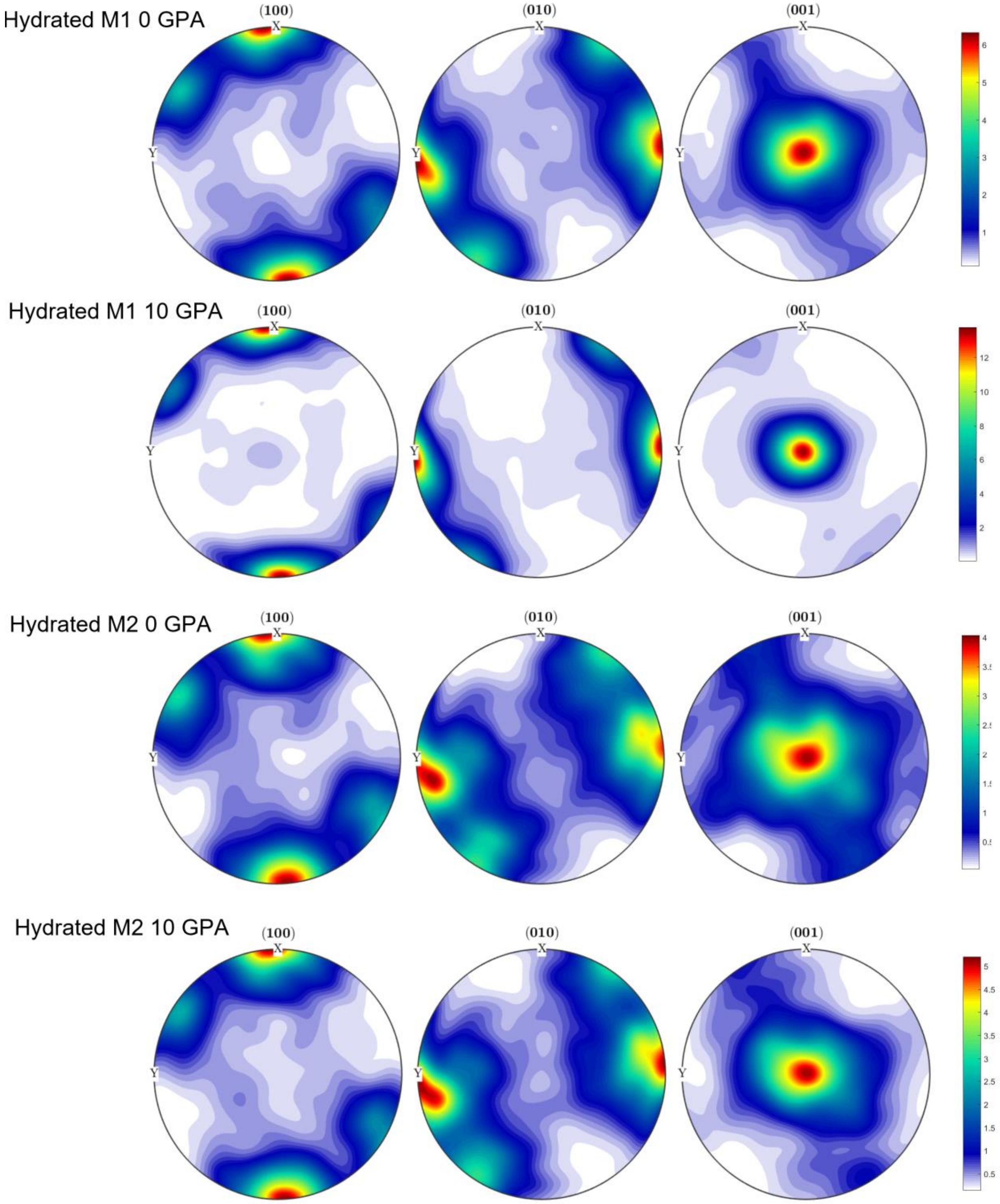

Figure 7: D-Rex simulations of forsterite textures with hydrated M1 and M2 vacancies near the slip plane at 0 and 10 GPa. Corrected Peierls stresses are used for the CRRS.

	Enthalpy of Reaction			Energy of Reaction (5 GPa, 1500 K)		
	0 GPa	5	10	1 ppm	100	1000
$\boldsymbol{V''_{M1} \rightarrow V''_{M2}}$	0.99	1.12	1.20	1.12	1.12	1.12
Reaction 1 Dry	6.72	6.64	6.56	8.55	7.95	7.65
Reaction 2 Dry	5.74	5.86	5.91	7.68	7.09	6.79
$\boldsymbol{2H^{x}_{M1} \rightarrow 2H^{x}_{M2}}$	0.54	0.63	0.79	0.63	0.63	0.63
Reaction 1 Wet	-0.32	-0.48	-0.59	1.42	0.83	0.53
Reaction 2 Wet	-1.51	-1.46	-1.38	0.44	-0.16	-0.46

Table 1: Energy (in eV) of converting an M1 vacancy to an M2 vacancy or Reaction 1 and 2 in dry or wet conditions with positive values representing the formation of M1 vacancies. The first three columns show the variation in enthalpy of the reaction as a function of pressure and the last three show the energy of the reaction at a specific temperature and pressure by adding the enthalpy to the calculated configurational entropy. These configurational entropy effects are invariant to pressure and scale with temperature. Vacancy concentrations are given in ppm H/Si- for dry vacancies which contain no H they are set to equivalent concentration of the wet vacancies.

	Dry			Wet		
	10 ppm	1000	10000	10 ppm	1000	10000
[100] M1	2.54	1.35	0.76	2.41	1.22	0.63
[100] M2	1.50	0.31	-0.28	0.95	-0.24	-0.83
[100] Si	-1.28	-1.87	-2.17	-0.61	-1.21	-1.50
[001] M1	2.65	1.46	0.87	2.52	1.33	0.74
[001] M2	1.52	0.33	-0.26	1.68	0.49	-0.10
[001] Si	-0.32	-0.92	-1.22	0.10	-0.50	-0.80

Table 2: Maximum energy gain (in eV) from moving a Mg or Si vacancy from a bulk environment to a [100] or [001] dislocation core. Vacancy concentrations are given in ppm H/Si- for dry vacancies which contain no H they are set to equivalent concentration of the wet vacancies. Some projections of vacancy distribution are shown in Fig 1 and S1.

Pressure	C11	C22	C33	C12	C13	C23	C44	C55	C66
0 GPa	298.1 GPa	184.0	217.1	60.7	63.0	68.5	62.0	78.5	76.1
5	333.2	209.7	244.2	79.6	80.8	83.4	72.1	82.8	82.7
10	366.5	231.3	268.0	99.3	99.8	100.7	79.4	87.9	90.8
	Errors								
0	2.1	1.9	1.8	1.3	1.1	0.9	0.7	0.8	0.6
5	2.2	1.9	1.4	1.1	0.9	0.8	1.2	0.9	0.5
10	2.0	1.8	1.9	1.1	1.3	0.8	0.8	0.8	0.4
	Anisotropic Energy Factors (eV/Å^3)								
	[100](010)		[001](010)		[100](001)		[001](100)		
	Edge	Screw	Edge	Screw	Edge	Screw	Edge	Screw	
0	0.0587	0.0347	0.0448	0.0384	0.0602	0.0341	0.0514	0.0341	
5	0.0646	0.0384	0.0506	0.0411	0.0657	0.0384	0.0562	0.0384	
10	0.0704	0.0415	0.055	0.0444	0.0708	0.0422	0.0605	0.0422	

Table 3: Calculated elastic constants (in GPa) and their errors for forsterite at 0, 5 and 10 GPa and static conditions.

		Peierls Stress (GPa)				Dislocation Width (Å)			
		[100](010)	[100](001)	[001](010)	[001](100)	[100](010)	[100](001)	[001](010)	[001](100)
Dry	Edge	1.91	4.98	2.36	4.31	6.72	3.84	9.56	8.47
	Screw	4.00	11.46	3.21	6.35	3.84	3.27	7.86	7.98
Mahendran et al. (2017)	Screw	3.1	7	7.2	6.9				
	Δ	-0.90	-4.46	3.99	0.56				
M1 (Hydrated)	Edge	1.71	3.55	1.96	4.42	6.63	4.04	9.44	8.23
	Screw	3.69	8.85	2.76	6.08	3.84	3.27	7.98	7.86
M2 (Hydrated)	Edge	1.66	4.10	2.18	6.17	9.32	4.23	24.80	8.23
	Screw	3.76	10.19	3.05	7.49	4.61	3.46	21.41	7.98
Si (Hydrated)	Edge	0.79	4.98	0.44	3.95	6.92	4.04	9.56	8.47
	Screw	2.26	10.16	0.63	4.43	3.94	3.27	8.11	7.98

Table 4: Calculated Peierls stress and dislocation width for 4 slip systems at 0 GPa with no vacancies and hydrated M1, M2 and Si vacancies. Also shown is the calculated screw Peierls stress from Mahendran *et al.* (2017) and the difference (Δ) between this value and our calculations.

	Peierls Stress (GPa)			Pressure Derivative of Peierls Stress At		
	0 GPa	5	10	0 GPa	5	10
Perfect						
[100](010)	4.00	5.67	6.27	0.44	0.34	0.23
[001](010)	7.21	6.44	5.90	-0.18	-0.15	-0.13
[001](001)	6.35	6.60	6.94	0.04	0.05	0.06
[100](001)	11.46	13.71	16.36	0.41	0.45	0.49
Wet						
[100](010)	4.87	5.76	6.22	0.22	0.18	0.14
[001](010)	6.90	6.55	6.12	-0.06	-0.07	-0.08
[001](001)	4.19	4.46	4.72	0.06	0.05	0.05
[100](001)	10.46	12.51	14.33	0.43	0.41	0.39

Table 5: Peierls stress of forsterite in perfect and wet (containing a hydrated Si vacancy) conditions and the pressure derivative of this stress as determined by fitting a polynomial to these points.

Supplementary Method:

Peierls-Nabarro:

To calculate dislocation glide in forsterite we use the Peierls-Nabbaro (PN) formalism (Nabarro, 1947). In this model a dislocation is represented as a distribution of partial dislocations along the glide plane. Two different forces determine the shape of the dislocation: the elastic interaction energies between atoms (which broaden the dislocation) and the inelastic misfit energy caused by the introduction of disregistry by forming a dislocation (which narrows the dislocation). At equilibrium these two forces balance and a dislocation width can be determined- this is the key output of the PN model. Once this has been established the Peierls stress can be determined.

Our Peierls-Nabarro (PN) calculations were done using the disloPy code (www.github.com/andreww/dislopy). This formulation represents a planar dislocation with finite core-width as a distribution of dislocation density ρ along the glide plane (see Bulatov and Cai (2006) for a complete treatment). The classical PN treatment requires a continuous dislocation density and misfit energy. This has two issues- 1) it is translationally invariant and so mobile under an infinitesimal external stress (and thus the Peierls stress is impossible to calculate) and 2) it is computationally difficult to calculate. Instead we shall use a semi-discrete formation (Bulatov and Kaxiras, 1997) where the dislocation is represented by a distribution of ρ on a discrete lattice and the inelastic energy is computed by summing over this lattice. This has the distinct advantage of being able to calculate the inelastic energy at a series of individual lattice points which can be done as a series of independent atomistic calculations rather than having to calculate the entire dislocation in a single calculation.

There are three key assumptions in this model- firstly that the non-linear interactions between adjacent partial dislocations are negligible, secondly that the core is relatively compact and thirdly that it is collinear. While the first two are likely to be true in forsterite the third is not for [001] screw dislocations- the breakdown of this assumption shall be revisited in the results and discussion sections.

To represent the two different forces two different functions need to be calculated in two separate calculations. To calculate the elastic interaction we need K, the elastic prefactor, which can be determined from the elastic constants of the appropriate crystal. These are calculated for forsterite with Density Functional Theory (DFT) as explained in the text. As forsterite is inherently anisotropic we then use the sextic formulation of Stroh (1958) to convert the elastic constants into an appropriate K for each slip system.

To determine the misfit energy we need to know the energy value of the function γ(u). This is called the γ-line in one direction and the γ-surface in two directions and is also called the Generalised Stacking Fault (GSF). This function gives the inelastic misfit energy of a crystal along the discrete lattice γ offset by the disregistry (u- the displacement of atoms from their perfect crystal positions). This is calculated with γ being set to the required dislocation vector in the required dislocation plane. To calculate the GSF we use a different set of DFT calculations. To do this we take a slab with long repetitions normal to the shear plane and then displace half of it various directions along γ and allow atoms to only relax normal to the shear plane. For each distance along γ the energy of the displaced slab is obtained, the energy of the crystal without displacement is subtracted, the remaining energy is divided by the surface area of the plane and then a γ(u) function is constructed.

With these two functions calculated the PN calculation proceeds as follows.

Firstly the dislocation density (ρ) is written in terms of the disregistry (u):

$\rho(x) = \frac{du(x)}{dx}$ Equation 1

Where x is the coordinate along the gamma surface (displacement direction of the dislocation).

The energy of the dislocation is then represented with Equation 2:

$E_{core} = E_{elastic} + E_{misfit} + E_{work}$ Equation 2

Where E_{misfit} is the inelastic energy, $E_{elastic}$ is the elastic energy and E_{work} is the work done on a dislocation by an applied stress (σ). These terms are then represented by:

$E_{work} = \sigma \int u(x)dx$ Equation 3

$E_{Elastic}[\rho(x)] = -K \iint \rho(x')\rho(x) ln|x - x'|dx'dx$ Equation 4

$E_{Misfit} = \sum_n \gamma(u(n))a_p$ Equation 5

In equation 4 K is the elastic prefactor defined above. In equation 5 a_p is the spacing between adjacent atomic planes and n are the grid points where calculations were done.

By setting Equation 3 to 0 (σ=0 no applied stress) the equilibrium disregistry function u(x) (static core structure) can be calculated by minimising E_{core} in Equation 2. This minimisation is constrained by the fact that the sum of ρ(x) must equal the burgers vector b. To find the Peierls stress you then progressively increase σ and relax the disregistry at each step, eventually no minimum will be able to be found- ie the dislocation is completely mobile- and this will give you a Peierls stress (σ).

To solve equation 2 numerically the disregistry function u(x) needs to be found. We do this by representing it as the sum of arctargent functions (ie partial dislocations) using

$u(x) = \frac{b}{\pi}\sum_i A_i \arctan\left(\frac{x-x_{o,i}}{c_i}\right) - C\Big)$ Equation 6

Where b is the burger vector and C is b/2 for the component of misfit parallel to the Burgers vector and zero otherwise. I is an index for the number of functions used to solve Equation 5 and the parameters A_i, $x_{0,i}$ and c_i are found by minimising E_{core} in Equation 2. The procedure is then:

1) Represent Equation 2 with equations 3, 4 and 5 with σ (and thus equation 3) set to 0
2) Represent the disregistery (u(x)) in equation 4 and 5 with equation 6
3) Numerically minimise the solution to Equation 2 by varying the parameters of equation 6 with constraint that the sum of ρ(x)=b
4) Obtain equilibrium disregistry

5) Increase the σ in Equation 2
6) Minimise equation 2 starting from the current parameters to equation 6
7) Repeat 5 and 6 until no minimum is obtained- Peierls stress

Si vacancy segregation:

To calculate the segregation of vacancies to clusters we first need to model a dislocation. This is too large to be modelled with DFT and so instead we use a forcefield based method. All segregation calculations were done with GULP (Gale, 1997) and the a forcefield designed for wet olivine (Wright and Catlow, 1994). Construction of the dislocation cores and of the segregation maps was done with the disloPy code (www.github.com/andreww/dislopy).

The potential that we used models cations with a formal charge (Mg 2+, Si 4+) whereas O atoms are modelled as a positively charged core (+0.84819) with a negatively charged massless shell (-2.84819). All cation-anion pairs are joined by a Buckingham potential and SiO_4 tetrahedra are fixed with a harmonic three body potential with details of this given in Table S1.

To prevent dislocation-dislocation interactions which are often large we instead use a 1D periodic cylinder which is periodic along the dislocation line and contains the dislocation in its centre. This cylinder has two radii- the first (R_1) contains the dislocation and its surrounding atoms, the second (R_2) contains atoms fixed in their bulk positions to simulate a perfect crystal.

Dislocation cores were constructed as in work (Skelton and Walker 2017)with the same cores and dislocation centres found. Dislocation core energies were found to converge (within 10 meV/ $Å^2$) at R_1= 25 Å for [100](010) edge and [100] and [001] screw dislocations and at R_1= 35 Å for [001](010) edge dislocations. [100](001) and [001](100) edge dislocations were not addressed in work (Skelton and Walker 2017)- their most stable cores were found to be at [0.74775,0.5] and [0.25,0.50225] and the energy of their cores converged when R_1 was set to 25 and 35 Å respectively. Columbic energy was calculated using the Wolf sum (Wolf et al., 1999) which generally gives more physically reasonable properties for systems without 3D periodic boundaries and its cutoff was set to 15 Å with a damping parameter x=0.2 $Å^{-1}$. The effect of the atoms fixed in their bulk positions in the outer circle cannot extend beyond the columbic cutoff and so R_2 was simply set to R_1+15 Å. The cluster needs to be repeated along the periodic dimension and this was done 4 times for Si vacancies with dislocation line vector [001] and 5 times for those with dislocation line vector [100]. The minimum distance between Si vacancies and their periodic repeat unit was 23.91 Å and 23.95 Å in the [100] and [001] orientated dislocations respectively.

The segregation energy of a defect is defined as the energy of reaction from taking it from a site in the bulk of the crystal and placing it near a dislocation core. In other words: $E_{seg} = \Delta E_{site-bulk} - \Delta E_{defect}$ Equation 7

Where ΔE_{defect} is the excess energy of the defect in the bulk and $\Delta E_{site\text{-}bulk}$ is the excess energy of a site compared to a site in the bulk. $\Delta E_{site\text{-}bulk}$ is calculated simply by removing a Mg or Si from each possible site in a different run and then comparing the energy of the different runs and ΔE_{defect} is calculated from 3D periodic boundary calculations.

Configurational Entropy of Vacancies

There are two major forms of configurational entropy in olivine. The first is site dependant and simply depends on the ratio of Mg vacancies to Mg sites or Si vacancies to Si sites. The second only occurs in hydrated olivine and concerns the arrangements of hydrogen in the vacancy.

For the distribution of Si vacancies in the bulk we can simply use Boltzmann's entropy:

$S = kblnW$ Equation 8

Where W is the amount of ways the system can be arranged. To solve this for Si vacancies in the bulk we used Stirling's approxmation

$S = NlnN - (N - n_{vac})\ln(N - n_{vac}) - n_{vac}lnn_{vac}$ Equation 9

Where N is the total number of Si sites and n_{vac} is the number of Si vacancies.

For Mg vacancies there are two non-equivalent sites and thus we must use the Gibbs entropy formulation:

$S = -kb\sum_i p_i\, lnp_i$ Equation 10

Where p_i is the probability of the occurrence of each microstate i. This is determined by

$p_i = \frac{1}{Z}e^{(-\frac{E_i}{KT})}$ Equation 11

Where Z is the canonical partition function

$Z = \sum_i e^{(-\frac{E_i}{KT})}$ Equation 12

For the different vacancy sites the energy of the microstates with vacancies on M1 or M2 respectively were taken from Table 1. For vacancies at dislocation cores they are pinned to a specific site and so this term was set to 0. Strictly there is a multitude of sites near dislocation core and their energy should be formulated, their effect on dislocation glide tallied and their distribution calculated but this is a simplified model that captures the partitioning of vacancies to the most stable dislocation core site and the effect of this vacancy on the core glide dynamics.

To calculate the configurational entropy of hydrogen in the vacancy we again use a Gibb's distribution (Equation 10-12). The microstates and their energies in this case were taken directly from Qin et al. (2018).

The effect of configurational entropy on Peierls-Nabarro calculations:

An additional consideration when dealing with hydrated vacancies is the loss of symmetry and thus configurational entropy caused by displacements (and in some case destruction) of the MgO_6 and SiO_4 tetrahedra. In the general sense this is dealt with by letting hydrogen find the minimum energy arrangement. As the Peierls-Nabarro model does not have a temperature component this should be sufficient. Real displacements happen at temperature, however, and breaking the equivalence of various hydrogen arrangements may incur an energy penalty, through loss of configurational entropy, not adequately accounted for by the model.

To examine the effect of this we took a sample case- [100](010) slip with an M2 vacancy. This was chosen because the M2 octahedra containing the vacancy is split during displacement and thus this system will show the maximum effect of configurational entropy. With this case we applied our PN model in two different ways. Firstly we did a standard GSF calculation which assumes no change in configurational entropy throughout and allows the H atoms to relax freely. Secondly we calculated the γ-line maximum and minimums of all 9 hydrogen arrangements (with hydrogen fixed to a specific O site but allowed to relax in that site) and then created a single γ-line maximum and minimum by using the Gibbs entropy formula (Equation 10-12) to partition the energy of all 9 individual pathways.

What was found was that displacing the crystal causes the most stable H configuration to be considerably more favoured than when compared to the undisplaced cell. At the γ-line minimum (undisplaced unit cell) the energies from different H configurations range from 0 to 0.83 eV with the nearest configuration to the minimum energy configuration being at 0.05 eV- nearly identical. At the gamma-line maximum (where the unit cell is at its most distorted) the range of energies for different H configurations now range from 0-4.48 eV with the nearest energy to the minimum configuration being at 0.68 eV. This vast discrepancy is because all of the H configurations except the most stable have H bonds across the shear plane and thus are strongly disrupted by shear. This means that when considering the statistical distribution of H arrangements, the most stable arrangement is overwhelmingly dominant and this is what is calculated in the regular GSF calculation. The difference in in GSF maximum from our standard calculation and from a calculation with explicit entropy consideration was found to be less than 5 meV/ $Å^2$ at 1500 K which is about equal to the error we obtain from not having infinite layers. Thus this is not a significant effect and shall be ignored.

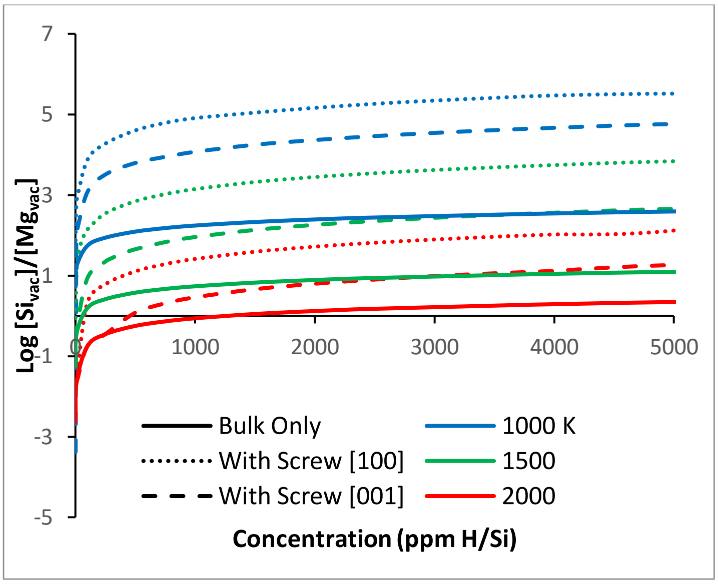

Figure S1: Ratio of the concentration of wet Si vacancies compared to wet Mg vacancies (M1+M2) for a varying water content at 5 GPa, in the presence of periclase (Reaction 2) and at different temperatures (1000, 1500 and 2000 K blue green and red respectively). Three different cases are shown- one with a pure bulk system (solid lines) and two with either a [100] screw dislocation core (dotted lines) or a [001] screw dislocation core (dashed lines) that vacancies can partition to. The systems with dislocation cores at some concentration develop excess Si vacancies- these Si vacancies are the one that partition to the dislocation core.

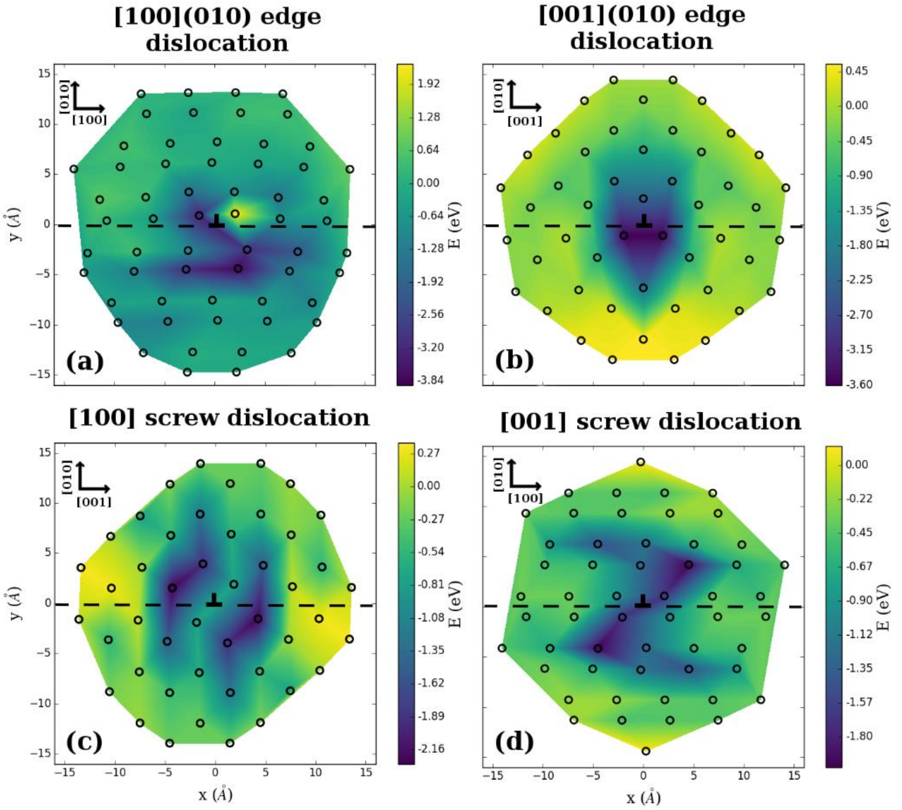

Fig S2: Contoured segregation energies of a V_{Si}'''' in the presence of a A) [100](010) edge dislocation B) [001](010) edge dislocation C) [100] screw dislocation and D) [001] screw dislocation in forsterite at 0 GPa calculated with the force field cluster method.

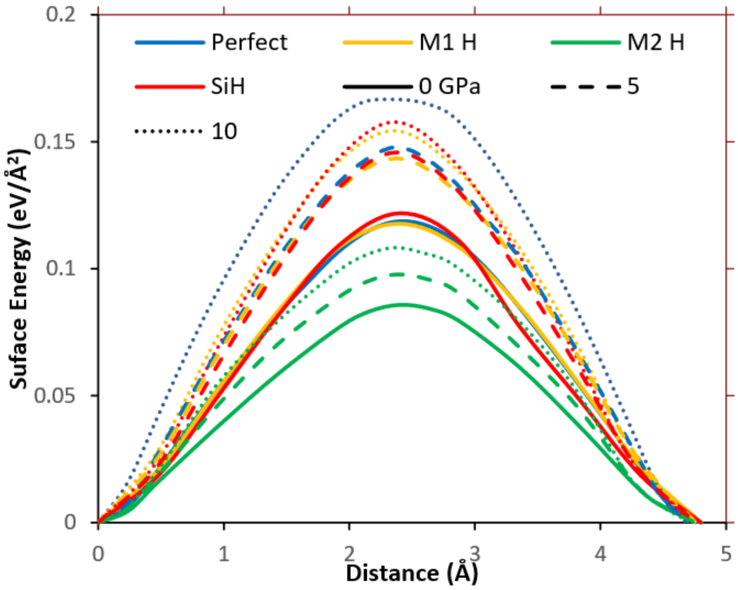

Fig S3: γ-lines for the [100](010) slip system with forsterite containing no vacancies (blue), hydrated M1 vacancies (orange), hydrated M2 vacancies (green) and hydrated Si vacancies (red) at 0 (solid line), 5 (dashed line) and 10 GPa (dotted line). Non-hydrated vacancies are not shown but typically look similar to those of the hydrated vacancies.

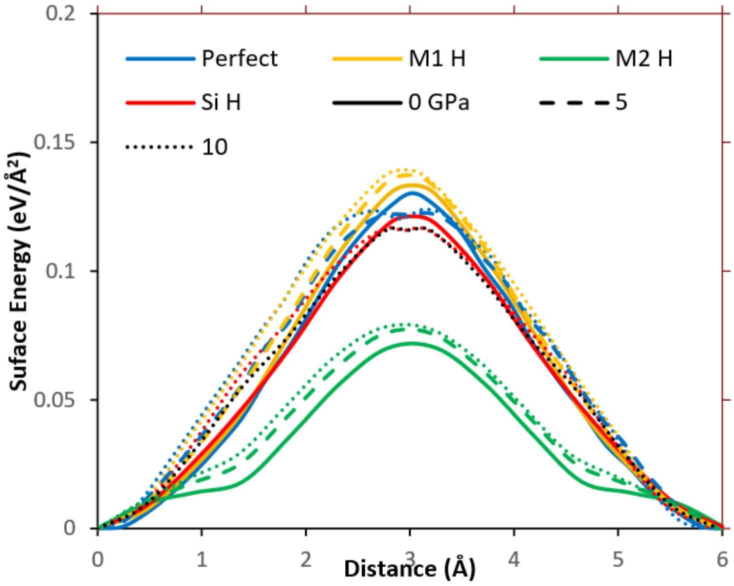

Figure S4: As Figure S3 but for the [001](010) slip system. The hydrated M2 vacancy has a considerably different shape and height to the other vacancies. With increasing pressure the no-vacancy and hydrated Si vacancy systems start to dissociate into two peaks slightly.

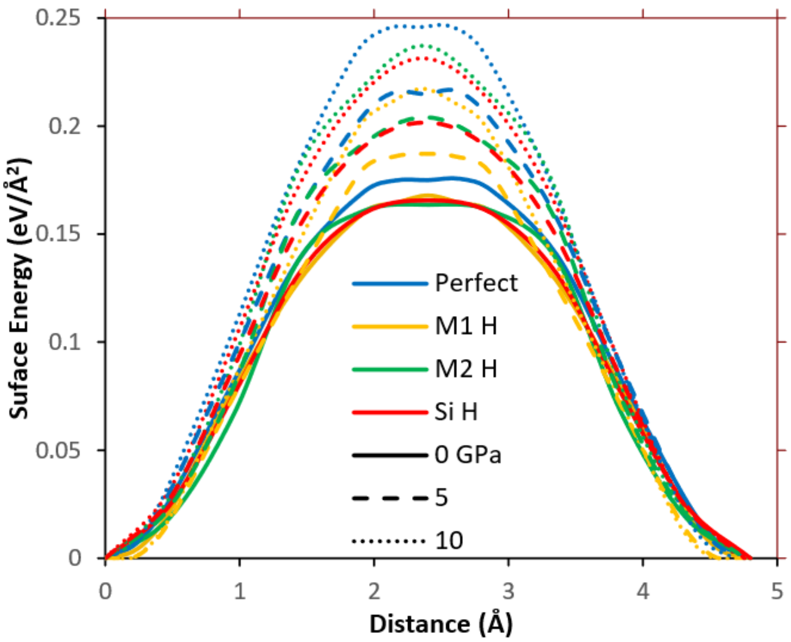

Figure S5: As Figure S3 but for the [100](001) slip system.

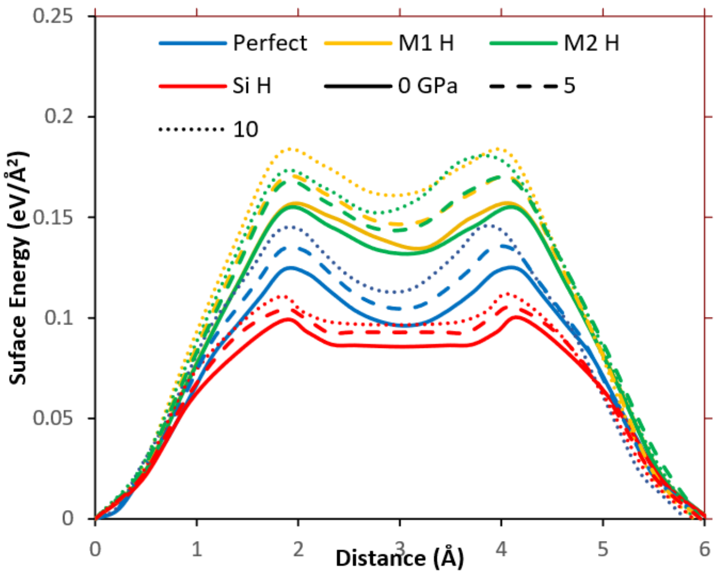

Figure S6: As Figure S3 but for the [001](100) slip system. The dissociated nature of these peaks remain fairly constant with pressure and with vacancies.

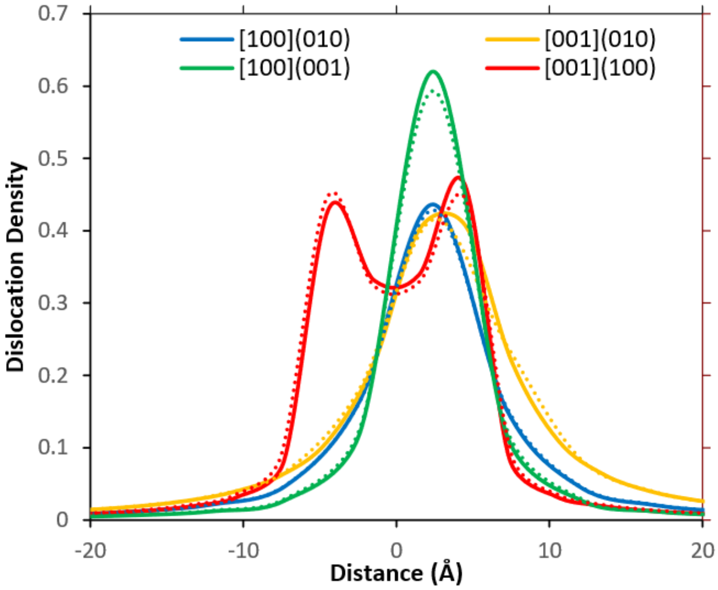

Figure S7: Edge dislocation density plots for forsterite containining no vacancies (solid line) and hydrated Si vacancies (dotted line) for the [100](010), [001](010), [100](001) and [001](100) slip systems at 0 GPa. Pressure had little effect on the shape of these plots.

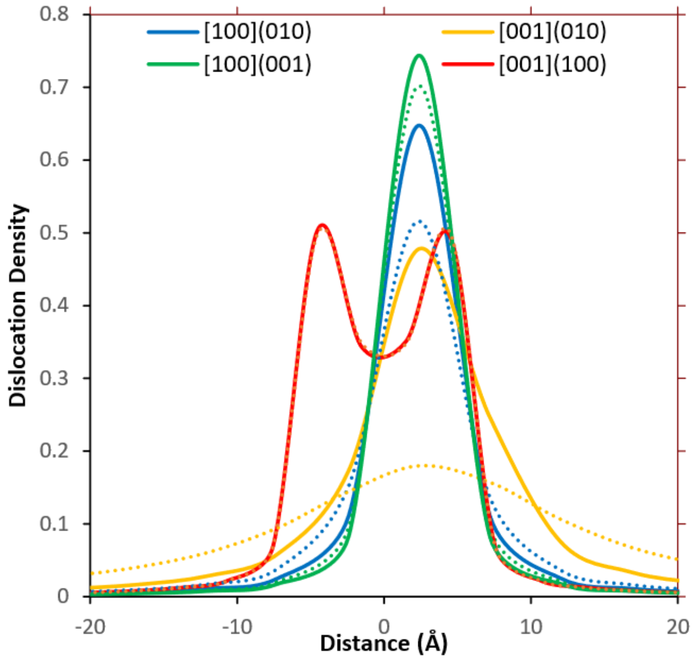

Figure S8: Screw dislocation density plots for forsterite containing hydrated M1 vacancies (solid line) and hydrated M2 vacancies (dotted line) for the [100](010), [001](010), [100](001) and [001](100) slip systems at 0 GPa. Pressure had little effect on the shape of these plots.

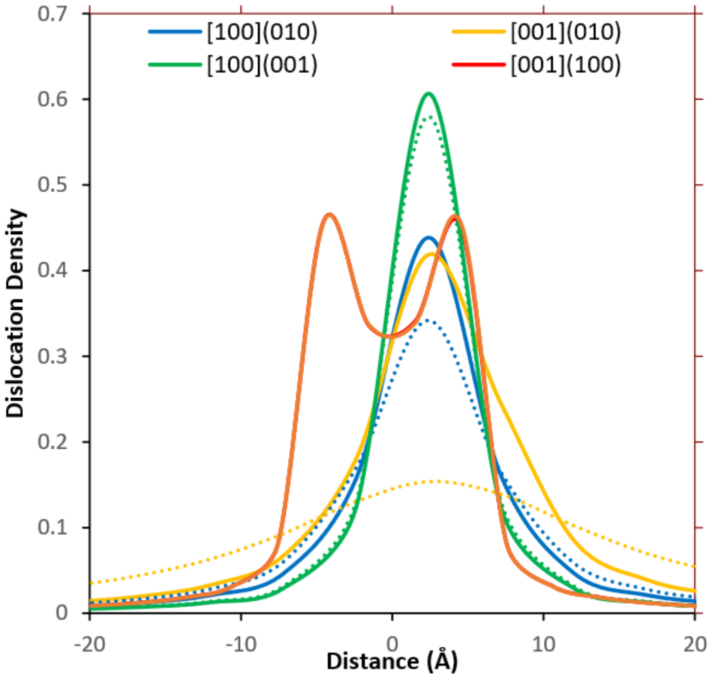

Figure S9: As Figure S8 but for edge dislocations.

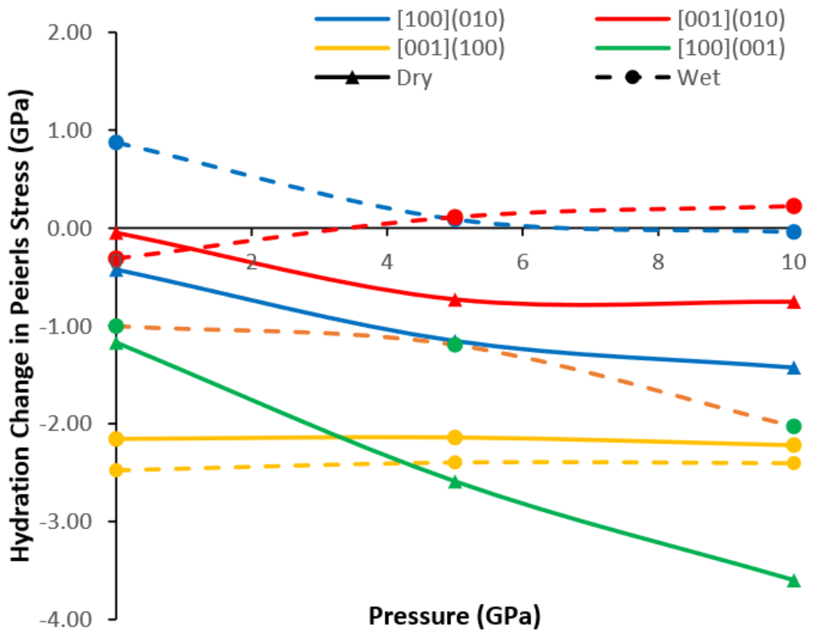

Figure S10: Change in screw Peierls stresses (from the bulk crystal) by adding wet (dashed) or dry Si vacancies near the slip plane in the 4 slip systems.

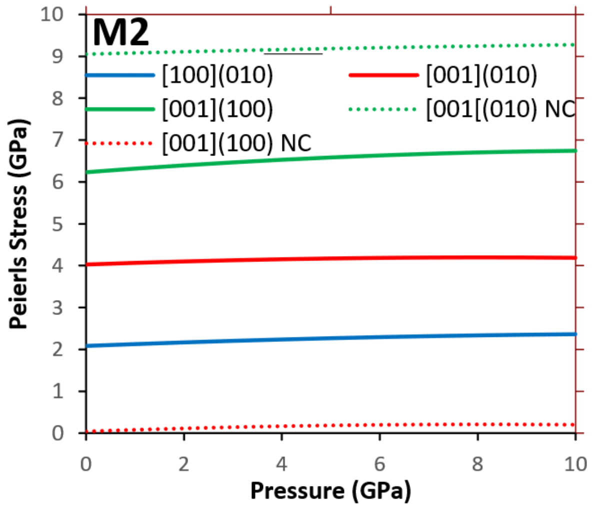

Figure S11: Plot of the Peierls stress of the screw dislocations with a hydrated M2 vacancy near the slip plane as a function of pressure for 4 slip systems. Two lines are shown for the slip systems with [001] Burgers vector- the dotted line is our calculated value whereas the solid line is our corrected value as discussed in the text.

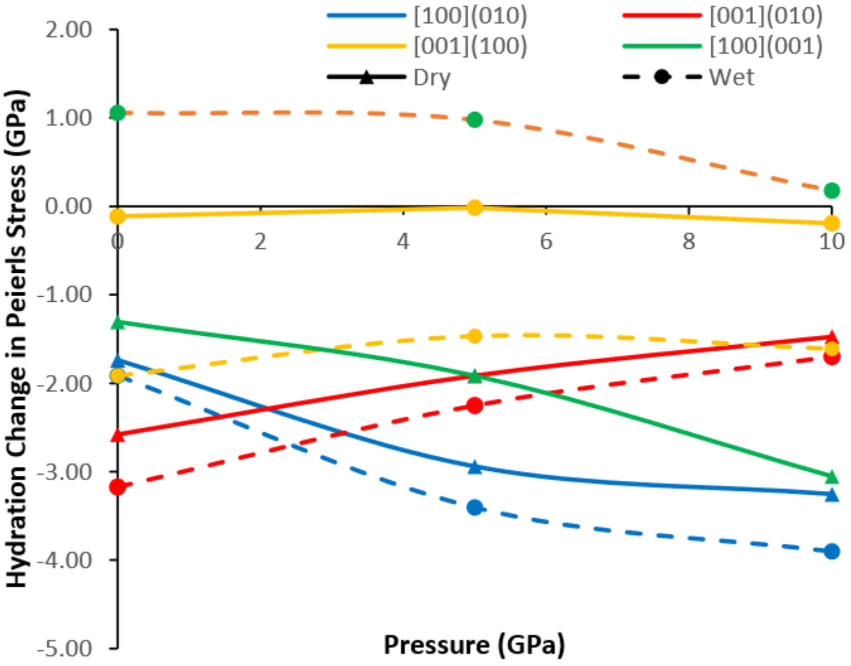

Figure S12: Change in screw Peierls stresses (from the bulk crystal) by adding wet (dashed) or dry M2 vacancies near the slip plane in the 4 slip systems.

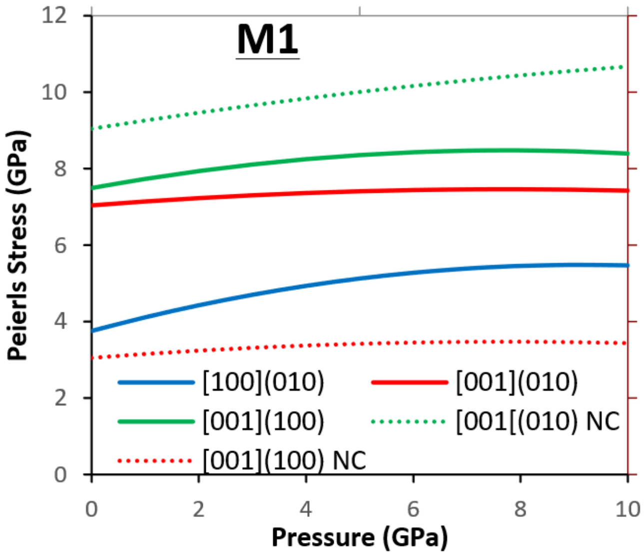

Figure S13: Plot of the Peierls stress of the screw dislocations with a hydrated M1 vacancy near the slip plane as a function of pressure for 4 slip systems. Two lines are shown for the slip systems with [001] Burgers vector- the dotted line is our calculated value whereas the solid line is our corrected value as discussed in the text.

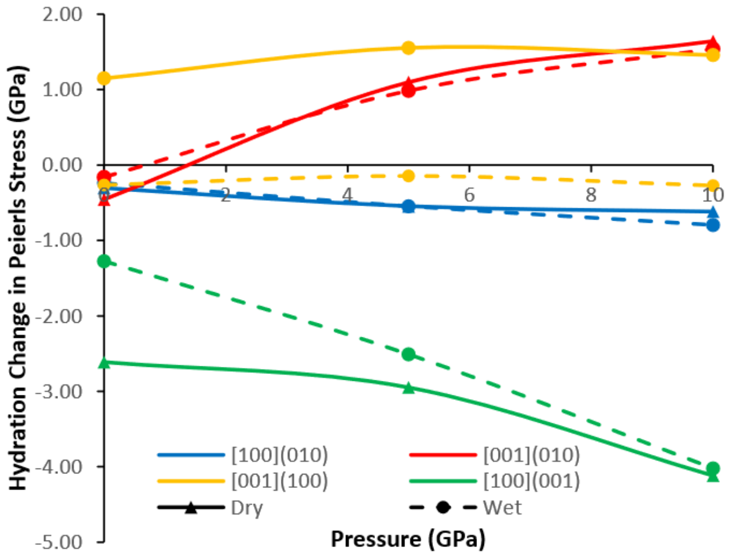

Figure S14: Change in screw Peierls stresses (from the bulk crystal) by adding wet (dashed) or dry M1 vacancies near the slip plane in the 4 slip systems.

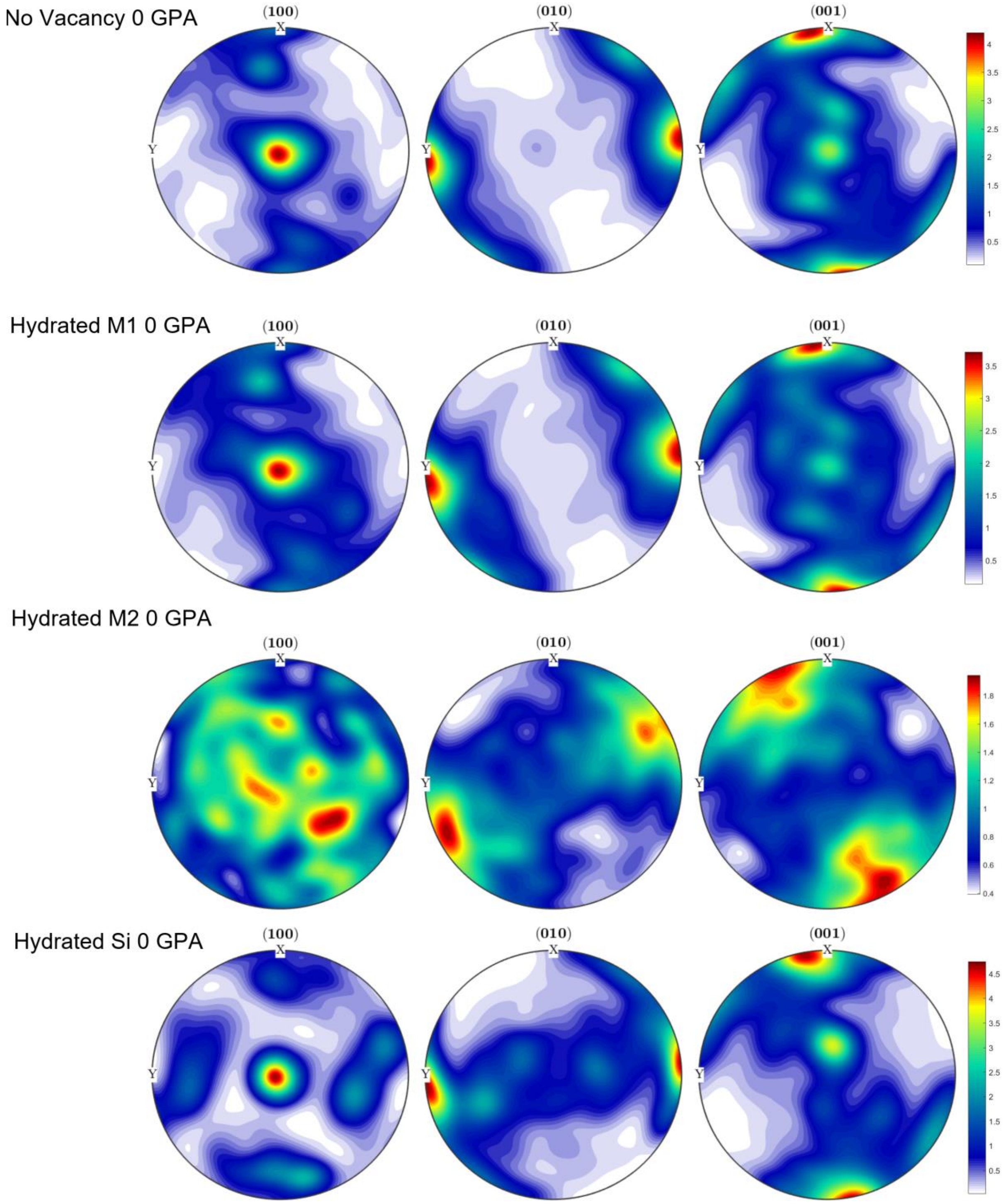

Figure S15: DRex fabric simulations of uncorrected Peierls stresses with no vacancies and hydrated M1, M2 and Si vacancies.

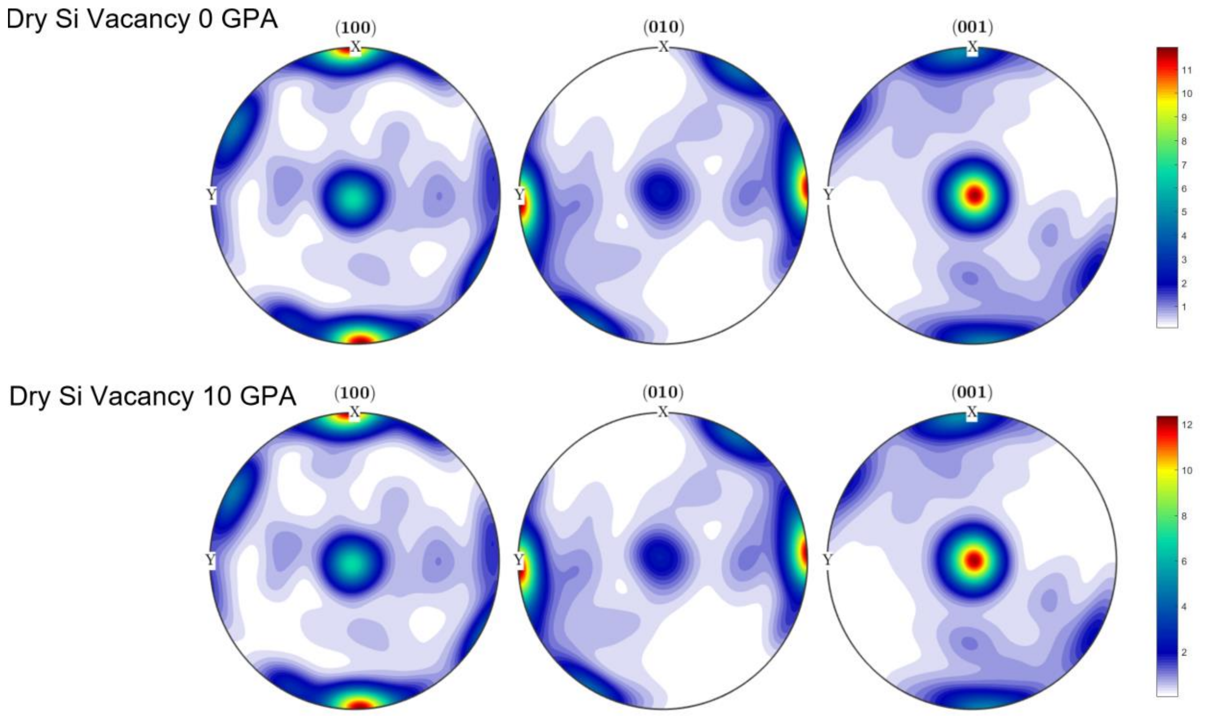

Figure S16: D-Rex fabric simulations of corrected Peierls stresses of forsterite with dry (non-hydrous) Si vacancies.

	Atoms		
	q_{core} (eV)	q_{shell} (eV)	
Mg	2.0	n/a	
Si	4.0	n/a	
O	0.84819	-2.84819	
O_H	-1.426	n/a	
H	0.426	n/a	
	Buckingham Potential		
	A (eV)	ρ (Å)	C_{ij} (eV*Å^6)
Mg-O	1428.5	0.29435	0
Mg-O_H	1060.5	0.29435	0
Si-O	1283.907	0.32052	10.66158
Si-O_H	983.556	0.32052	10.66128
O^*-O^*	22764	0.149	27.88
O^*-H^b	311.96	0.25	0
	Morse		
	D_e (eV)	A (Å^{-1})	r_0 (Å)
H-OH	7.02525	2.03	0.9485
	Three Body		
	k3 (eV rad^{-2})	Θ_0(°)	
O^*-Si-O^*	2.0972	109.47	
	Spring		
	k2 (eV Å^{-2})		
O_{core}-O_{shell}	74.92038		

Table S1 Potentials used in our forcefields calculations. O (the normal oxygen in the crystal lattice) and O_H (the oxygen in a hydroxyl group) have some unique but also some shared forcefields- O* represents both O and O_H. The Morse potential for O_H-H interactions was set to operate between 0 and 1.5 Å whereas the Buckingham potential for O-H interactions was set to operate between 1.5-10 Å. This ensures (with a sensible starting geometry) that the O-H bond is modelled by a Morse potential but the interaction of the oxygen in the OH group with the other Hydrogen in the vacancy is modelled with a Buckingham potential. If both potentials are set to operate from 0- 10 Å then the hydrogen atoms either fall outside of the vacancy or into the centre of the vacancy (depending upon starting geometry) which does not match the more accurate predictions of DFT.

	[100](010)			[001](010)			[001](001)			[100](001)		
	0 GPa	5	10	0	5	10	0	5	10	0	5	10
Perfect	4.00	5.67	6.23	3.21	2.44	1.90	6.35	6.60	6.94	11.46	13.71	16.36
M1 Dry	3.69	5.13	5.65	2.76	3.53	3.54	6.08	6.46	6.67	8.85	10.76	12.24
M1 Wet	3.76	5.13	5.47	3.05	3.42	3.44	7.49	8.16	8.40	10.19	11.20	12.34
M2 Dry	2.26	2.73	3.01	0.63	0.52	0.43	4.43	5.14	5.33	10.16	11.79	13.31
M2 Wet	2.08	2.27	2.36	0.04	0.18	0.20	6.23	6.59	6.75	12.52	14.68	16.53
Si Dry	3.57	4.52	4.84	3.16	1.71	1.15	3.87	4.21	4.53	10.29	11.12	12.76
Si Wet	4.87	5.76	6.22	2.90	2.55	2.12	4.19	4.46	4.72	10.46	12.51	14.33

Table S2: Collection of Peierls stresses (in GPa) at three pressures (0, 5, 10 GPa) for the screw dislocation in 4 slip systems with no vacancies and with hydrous or nonhydrous M1 or M2 or Si vacancies.

		Peierls Stress (GPa)			Max GSF Energy (eV/Å^2)			E_{core} (eV)			Width (Å)		
		0 GPa	5	10	0	5	10	0	5	10	0	5	10
Perfect	Edge	1.91	3.37	4.48	0.115	0.143	0.166	-1.14	-0.93	-0.78	6.73	4.76	4.25
	Screw	4.00	5.67	6.23				-0.31	-0.18	-0.09	3.84	3.43	3.21
M1-Dry	Edge	1.71	2.68	3.09	0.119	0.145	0.156	-1.07	-1.06	-1.04	6.34	5.24	5.01
	Screw	3.69	5.13	5.65				-0.28	-0.24	-0.22	3.65	3.52	3.40
M1-Wet	Edge	1.66	2.68	2.92	0.118	0.143	0.154	-1.13	-1.07	-1.05	6.63	5.24	5.01
	Screw	3.76	5.13	5.47				-0.31	-0.24	-0.22	3.84	3.52	3.40
M2-Dry	Edge	0.79	1.00	1.22	0.095	0.111	0.121	-1.36	-1.31	-1.29	8.26	7.24	6.80
	Screw	2.26	2.73	3.01				-0.42	-0.36	-0.33	4.23	3.90	3.69
M2-Wet	Edge	0.79	0.94	0.98	0.086	0.098	0.108	-1.52	-1.50	-1.48	9.32	8.57	8.03
	Screw	2.08	2.27	2.36				-0.51	-0.47	-0.42	4.61	4.29	4.06
Si-Dry	Edge	0.99	1.67	1.88	0.114	0.135	0.146	-1.15	-1.09	-1.04	6.73	5.71	5.67
	Screw	3.57	4.52	4.84				-0.33	-0.30	-0.28	3.84	3.62	3.59
Si-Wet	Edge	2.40	2.97	3.19	0.122	0.146	0.158	-1.20	-1.08	-1.11	6.92	5.52	5.29
	Screw	4.87	5.76	6.22				-0.36	-0.28	-0.27	3.94	3.62	3.59

Table S3: Collection of Peierls Stress, maximum energy of the γ line, core energy (E_{core} in equation 2), dislocation width and dislocation centre for the [100](010) dislocations.

		Peierls Stress (GPa)			Max GSF Energy (eV/Å^2)			E_{core} (eV)			Width (Å)		
		0 GPa	5	10	0	5	10	0	5	10	0	5	10
Perfect	Edge	2.36	1.63	1.23	0.130	0.122	0.120	-2.16	-2.13	-2.08	9.56	9.43	8.73
	Screw	3.21	2.44	1.90				-1.60	-1.46	-1.38	7.86	6.80	6.02
M1-Dry	Edge	1.96	2.48	2.52	0.129	0.133	0.137	-2.02	-2.15	-2.20	9.19	9.07	8.96
	Screw	2.76	3.53	3.54				-1.55	-1.51	-1.49	7.74	7.28	7.20
M1-Wet	Edge	2.18	2.33	2.48	0.133	0.137	0.139	-2.28	-2.18	-2.10	9.44	9.19	8.49
	Screw	3.05	3.42	3.44				-1.61	-1.51	-1.41	7.98	7.28	6.61
M2-Dry	Edge	0.44	0.36	0.30	0.070	0.080	0.084	-2.34	-2.38	-2.50	11.98	11.10	10.9
	Screw	0.63	0.52	0.43				-1.60	-1.63	-1.69	10.52	9.31	9.20
M2-Wet	Edge	0.02	0.04	0.06	0.070	0.076	0.078	-3.53	-3.56	-3.68	24.80	20.29	19.3
	Screw	0.04	0.18	0.20				-2.46	-2.59	-2.64	21.41	15.99	15.1
Si-Dry	Edge	2.48	0.97	0.65	0.112	0.115	0.118	-2.02	-1.96	-1.94	9.44	8.83	8.73
	Screw	3.16	1.71	1.15				-1.55	-1.41	-1.33	8.35	6.68	6.61
Si-Wet	Edge	2.18	1.79	1.30	0.121	0.116	0.116	-2.05	-2.17	-2.29	9.56	9.43	9.35
	Screw	2.90	2.55	2.12				-1.47	-1.49	-1.55	8.11	7.64	7.58

Table S4: As table S3 but for [001](010) dislocations

		Peierls Stress (GPa)			Max GSF Energy (eV/Å^2)			E_{core} (eV)			Width (Å)		
		0 GPa	5	10	0	5	10	0	5	10	0	5	10
Perfect	Edge	4.98	7.47	9.67	0.175	0.215	0.246	-0.66	-0.63	-0.62	3.84	3.81	3.59
	Screw	11.46	13.71	16.36				-0.09	-0.07	-0.06	3.27	3.24	3.21
M1-Dry	Edge	3.55	5.18	6.63	0.169	0.197	0.224	-0.88	-0.83	-0.80	4.32	4.09	3.97
	Screw	8.85	10.76	12.24				-0.20	-0.17	-0.15	3.46	3.24	3.21
M1-Wet	Edge	4.10	5.34	6.78	0.168	0.187	0.217	-0.68	-0.87	-0.88	4.04	4.19	3.97
	Screw	10.19	11.20	12.34				-0.09	-0.20	-0.21	3.27	3.33	3.31
M2-Dry	Edge	4.98	5.52	7.39	0.179	0.198	0.232	-0.74	-0.75	-0.75	4.04	4.00	3.87
	Screw	10.16	11.79	13.31				-0.12	-0.14	-0.14	3.27	3.24	3.21
M2-Wet	Edge	4.24	6.68	8.61	0.164	0.204	0.237	-0.94	-0.90	-0.87	4.23	4.00	3.78
	Screw	12.52	14.68	16.53				-0.30	-0.26	-0.23	3.46	3.43	3.21
Si-Dry	Edge	4.48	4.99	6.43	0.178	0.192	0.216	-0.74	-0.75	-0.76	4.04	4.00	3.87
	Screw	10.29	11.12	12.76				-0.13	-0.13	-0.14	3.27	3.24	3.21
Si-Wet	Edge	3.93	5.95	7.77	0.166	0.202	0.231	-0.76	-0.72	-0.68	4.04	3.81	3.78
	Screw	10.46	12.51	14.33				-0.15	-0.12	-0.10	3.27	3.24	3.21

Table S5: As table S3 but for [100](001) dislocations

		Peierls Stress (GPa)			Max GSF Energy (eV/Å^2)			E_{core} (eV)			Width (Å)		
		0 GPa	5	10	0	5	10	0	5	10	0	5	10
Perfect	Edge	4.31	4.62	4.98	0.124	0.134	0.143	-1.99	-2.10	-2.18	8.47	8.36	8.26
	Screw	6.35	6.60	6.94	0.096	0.105	0.113	-0.97	-1.08	-1.15	7.98	7.88	7.78
M1-Dry	Edge	4.42	4.57	4.68	0.118	0.120	0.123	-2.00	-2.12	-2.22	8.47	8.36	8.26
	Screw	6.08	6.46	6.67	0.089	0.093	0.097	-0.99	-1.10	-1.19	7.98	7.88	7.78
M1-Wet	Edge	6.17	7.07	7.48	0.155	0.169	0.182	-1.64	-1.70	-1.74	8.23	8.12	8.02
	Screw	7.49	8.16	8.40	0.135	0.148	0.163	-0.70	-0.75	-0.80	7.86	7.88	7.78
M2-Dry	Edge	3.95	3.75	3.61	0.118	0.122	0.126	-2.02	-2.20	-2.35	8.47	8.48	8.49
	Screw	4.43	5.14	5.33	0.091	0.096	0.101	-1.00	-1.15	-1.28	7.98	8.00	8.02
M2-Wet	Edge	6.18	6.55	6.72	0.154	0.166	0.172	-1.66	-1.83	-1.86	8.23	8.12	8.02
	Screw	6.23	6.59	6.75	0.133	0.146	0.159	-0.70	-0.81	-0.88	7.98	7.76	7.78
Si-Dry	Edge	1.72	1.92	2.04	0.087	0.096	0.101	-2.29	-2.38	-2.49	8.71	8.59	8.49
	Screw	3.87	4.21	4.53	0.058	0.066	0.070	-1.23	-1.32	-1.42	7.98	8.00	8.02
Si-Wet	Edge	2.56	2.70	2.86	0.099	0.104	0.111	-1.97	-2.07	-2.16	8.47	8.36	8.26
	Screw	4.19	4.46	4.72	0.086	0.093	0.096	-0.98	-1.08	-1.17	7.98	7.88	7.78

Table S6: As table S3 but for [001](100) dislocations. In this case two surface energies are reported- the first is the maximum value of the γ line and the latter is the minima between the two peaks in the γ line.

BULATOV, V. V. & CAI, W. 2006. *Computer Simulations of Dislocations, Oxford Series on Material Modelling*, Oxford University Press.

BULATOV, V. V. & KAXIRAS, E. 1997. Semidiscrete variational Peierls framework for dislocation core properties. *Physical Review Letters,* 78**,** 4221-4224.

GALE, J. D. 1997. GULP - a computer program for the symmetry adapted simulation of solids. *JCS Faraday Trans,* 93**,** 629-637.

NABARRO, F. R. N. 1947. DISLOCATIONS IN A SIMPLE CUBIC LATTICE. *Proceedings of the Physical Society of London,* 59**,** 256-272.

STROH, A. N. 1958. DISLOCATIONS AND CRACKS IN ANISOTROPIC ELASTICITY. *Philosophical Magazine,* 3**,** 625-&.

WOLF, D., KEBLINSKI, P., PHILLPOT, S. R. & EGGEBRECHT, J. 1999. Exact method for the simulation of Coulombic systems by spherically truncated, pairwise r(-1) summation. *Journal of Chemical Physics,* 110**,** 8254-8282.

WRIGHT, K. & CATLOW, C. R. A. 1994. A computer simulation study of (OH) defects in olivine. *Physics and Chemistry of Minerals,* 20**,** 515-518.